

Conductivity Optimization of Mg, Zn and Ag doped TiO₂ as Electron Transport Layer for Perovskite Solar Cell

Sameeksha Sharma

Panjab University

Nazilla Soleimanioun

Panjab University

Mamta Rani

DAV University

Surya Kant Tripathi (✉ surya@pu.ac.in)

Panjab University, Chandigarh <https://orcid.org/0000-0002-4955-8860>

Research Article

Keywords: Electron transport layer, Conductivity, Activation energy, Urbach energy, Binding energy

Posted Date: February 18th, 2021

DOI: <https://doi.org/10.21203/rs.3.rs-203949/v1>

License:  This work is licensed under a Creative Commons Attribution 4.0 International License.

[Read Full License](#)

Conductivity optimization of Mg, Zn and Ag doped TiO₂ as electron transport layer for Perovskite solar Cell

Sameeksha Sharma^(a), Nazilla Soleimanioun^(a), Mamta Rani^(b) and S. K. Tripathi^(a,*)

^aCentre of Advanced study in Physics, Department of Physics, Panjab University, Chandigarh 160 014, India

^bDepartment of Physics, DAV University, Jalandhar 144012, Punjab, India

*Corresponding author: surya@pu.ac.in

Abstract: We report on the modification of structural, optical, electrical and dielectric properties of the electron transport layer (ETL) of Perovskite solar cell (PSC) i.e. Titanium dioxide (TiO₂) by adding Magnesium (Mg), Zinc (Zn) and Silver (Ag) impurities in it through Sol-gel method. Modified parameters are studied with the help of X-Ray diffraction (XRD), UV-Visible (UV-Vis) spectroscopy, electrical and dielectric measurements by two probe method respectively. Fascinating results have been obtained in modified Mg-TiO₂, Zn-TiO₂ and Ag-TiO₂ such as enhanced transmittance (T), reduction in refractive index (n), extinction coefficient (k), Urbach energy (E_U), an increase in DC conductivity, dielectric constant (ε) and AC conductivity. The conductivity in modified TiO₂ follows the order Ag-TiO₂>Zn-TiO₂>Mg-TiO₂>TiO₂. The prepared samples are utilized in PSC device fabrication and the increased efficiency following the same order as conductivity suggests the idea of doping in ETL successful in solar cell application.

Keywords: Electron transport layer, Conductivity, Activation energy, Urbach energy, Binding energy.

1. Introduction

Doped semiconductors have received the attention of the researchers to utilize them in optical, catalytic and electrical applications. The presence of various crystalline polymorphs and morphologies make them suitable in various fields. Size-dependent properties help the researchers to modify their properties to the extent they want in a particular application. In the last decade, the production and consumption of titanium dioxide TiO_2 have been considerably increased due to its fascinating characteristics such as large availability, non-toxicity, low cost and optoelectronic properties [1].

TiO_2 crystallizes in various phases such as anatase, brookite and rutile where anatase phase possesses high conductivity in comparison to other existing phases. The formation of these phases is a function of temperature. At low temperature, the anatase phase occurs whereas, with an increase in temperature, the rutile phase starts to appear. It finds its application in the various research areas such as photocatalysis, memory devices, solar cells and, MOSFETs. TiO_2 material also acts as an electron transport layer (ETL) in case of third-generation Perovskite solar cells (PSCs) to help the electrons generated from light illumination of the active layer to reach the electrode easily [2]. Anatase phase is the desired phase in PSCs.

Nanostructured TiO_2 can be prepared by a variety of methods such as sol-gel method, hydrothermal method, physical vapor deposition [3], laser chemical vapor deposition [4]. An effective way to modify its electronic properties is through doping [1] i.e addition of impurities to TiO_2 lattice. Doping can be done either by replacing O^{2-} anion or Ti^{4+} cation. Cationic doping can be done by metals and anionic doping by non-metals. The lower side of the conduction band (CB) is constituted by Ti^{4+} 3d bands therefore replacement of Ti^{4+} metal ions tends to bring a change in CB structure. On the other edge, the upper side of the valence band (VB) is formed by O^{2-} 2p bands, thus anion doping tends to change the VB structure [5].

Here, we have used the Sol-Gel technique to prepare TiO_2 nanoparticles. The properties of prepared nanoparticles have been modified by dopants (Magnesium (Mg), Zinc (Zn) and Silver (Ag)) i.e Mg-TiO_2 , Zn-TiO_2 and Ag-TiO_2 . The ionic radii of Mg^{2+} (0.66 Å), Zn^{2+} (0.74 Å) and Ag^+ (1.15 Å) ions is comparable to Ti^{4+} (0.68 Å) ions. Therefore, these dopants can easily substitute Ti^{4+} in the TiO_2 matrix without any change in its basic crystal structure. The purpose is to examine the effect of doping of Mg, Zn and Ag on pristine TiO_2 as the electrical and optical properties of semiconducting materials are substantially modified by impurity doping

[6]. Structural properties of prepared films have been analyzed with the help of the XRD technique. UV-Vis spectroscopy is used to study the optical properties. Electrical and dielectric measurements have been done by the two-probe method to study current-voltage (I-V) characteristics and AC conductivity. After these characterizations, materials have been used as an ETL in PSC device fabrication.

2. Experimental details

The precursor's Titanium butoxide (Sigma Aldrich), Titanium isopropoxide (Sigma Aldrich), Acetic acid (CDH), Sulphuric acid (Qualikems), Hydrochloric acid (HCL), Magnesium nitrate (Loba) and ethanol were used for the synthesis. TiO_2 and doped Mg- TiO_2 , Zn- TiO_2 and Ag- TiO_2 nanoparticles were prepared by Sol-gel method following the procedure as shown in Fig. 1 [7]. The procedure was the same for other dopants as well. The Perovskite active layer material ($\text{CH}_3\text{NH}_3\text{PbI}_3$) was prepared following the reported procedure [8]: hydroiodic acid (6 mL, Sigma Aldrich) and methylamine (5.6 mL, Laboratory Rasayan) were stirred in an ice bath at 5 °C for 2 h. The resulting solution was evaporated at 50 °C for one hour to get $\text{CH}_3\text{NH}_3\text{I}$. The obtained precipitates were washed with diethyl ether three times and then dried at 100 °C in the oven. To prepare $\text{CH}_3\text{NH}_3\text{PbI}_3$, $\text{CH}_3\text{NH}_3\text{I}$ (159 mg) and PbI_2 (461 mg, Sigma Aldrich) were dissolved in 1 mL γ -butyrolactone at 60 °C for overnight with stirring. To prepare the hole transport layer (HTL) 6 mg of copper thiocyanate (CuSCN) (Sigma Aldrich) was dissolved in 1 mL of propyl sulphide (CDH).

For film deposition, at first, the substrates were washed sequentially with detergent, acetone and distilled water for 15 minutes each and followed with drying. Now the deposition of TiO_2 compact layer was done by the reported procedure [9]: Titanium isopropoxide (2.54 mL) was diluted in ethanol (16.9 mL) and 350 μL HCL was diluted in ethanol (16.9 mL). Two solutions were mixed by adding acidic solution dropwise into the titanium isopropoxide solution with stirring. The resulting solution was spun on to the fluorine-doped tin oxide (FTO) at rpm of 2000 for 60 sec and then the film was annealed at 500 °C. Mesoporous TiO_2 layer was deposited by spinning the solution of prepared nanoparticles in polyethylene glycol (PEG) at 5000 rpm for 60 sec [10] and annealed at 500 °C. For device fabrication, $\text{CH}_3\text{NH}_3\text{PbI}_3$ was deposited on mesoporous TiO_2 by spin coating at 2500 rpm for 30 sec and annealed at 50 °C for 10 minutes. After perovskite deposition, HTL was deposited by spin

coating the prepared solution at 2000 rpm for 60 sec. Thermal evaporation technique was used to deposit Gold contacts.

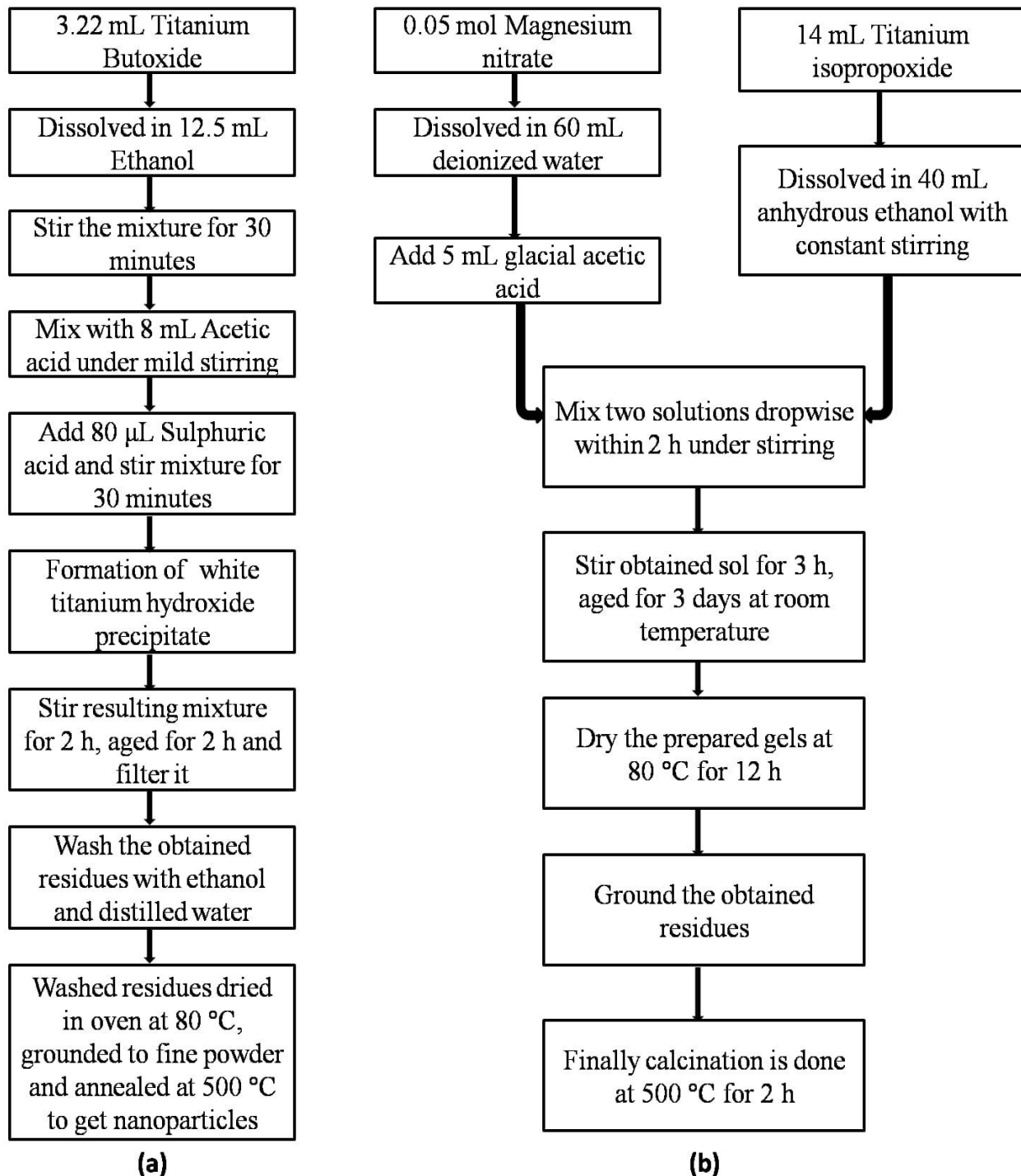


Fig. 1 Synthesis procedure for (a) TiO₂ nanoparticles. (b) doped TiO₂ nanoparticles.

X-ray diffraction pattern of the samples was studied with the help of Rigaku Miniflex-600 X-Ray diffractometer in 2θ range of 10° to 70° . Transmittance measurements were recorded with

double beam spectrophotometer Jasco v-630 in 300-800 nm range. To carry out the electrical and dielectric measurements, a metallic sample holder which was connected to a rotary vacuum pump to have a vacuum of $\approx 10^{-3}$ mbar was used for whole measurements. Keithley (6517A-a programmable voltage source) and picoammeter (DPM-111 model) were used to provide voltage (V) and measure current (I). Dark conductivities of these films were studied at different temperatures by using heaters which are connected to variac outside the sample holder to vary the rate of heating. The heating rate was displayed through the digital panel which was connected to the copper-constantan thermocouple. AC conductivity measurements were carried out with the help of Hioki 3532-50 LCR Hi-Tester in the frequency range of 50 Hz - 5 MHz.

3. Results and discussion

Fig. 2 illustrates the XRD profile of pristine TiO₂ and Mg-TiO₂, Zn-TiO₂ and Ag-TiO₂ films. The peaks observed for the prepared material represented by their hkl values (as shown in Fig. 2) describes the well crystalline behaviour expressed as the desired anatase phase with tetragonal crystal structure according to the JCPDS file 01-089-4921 for TiO₂. In addition to it, the peaks contributing to the substrate (FTO) are represented by the symbol '*'. No additional peak of dopants Magnesium (Mg), Zinc (Zn) and Silver (Ag) has been observed. This may be due to the small quantity of dopant or the good dispersion of dopant in pristine material [11] but the existence of dopants is observed in EDS results shown in Fig. 3. A shift in the position of the peaks has been noticed in the modified samples and is maximum for Zn-TiO₂ which may be due to the presence of strain introduced by the incorporation of dopant. The induced strain may be related to the broadening of the peak in the diffraction profile. Although several factors are responsible for peak broadening such as defects in crystal, instrumental error, stress, strain, orientation and finite crystal size but instrumental broadening have the major contribution to the broadening of peak [12]. The instrumental broadening should be reduced to its minimum value to have the corrected value of crystallite size. This can be done by considering peak width as the contribution of both samples as well as instrument dependent effects.

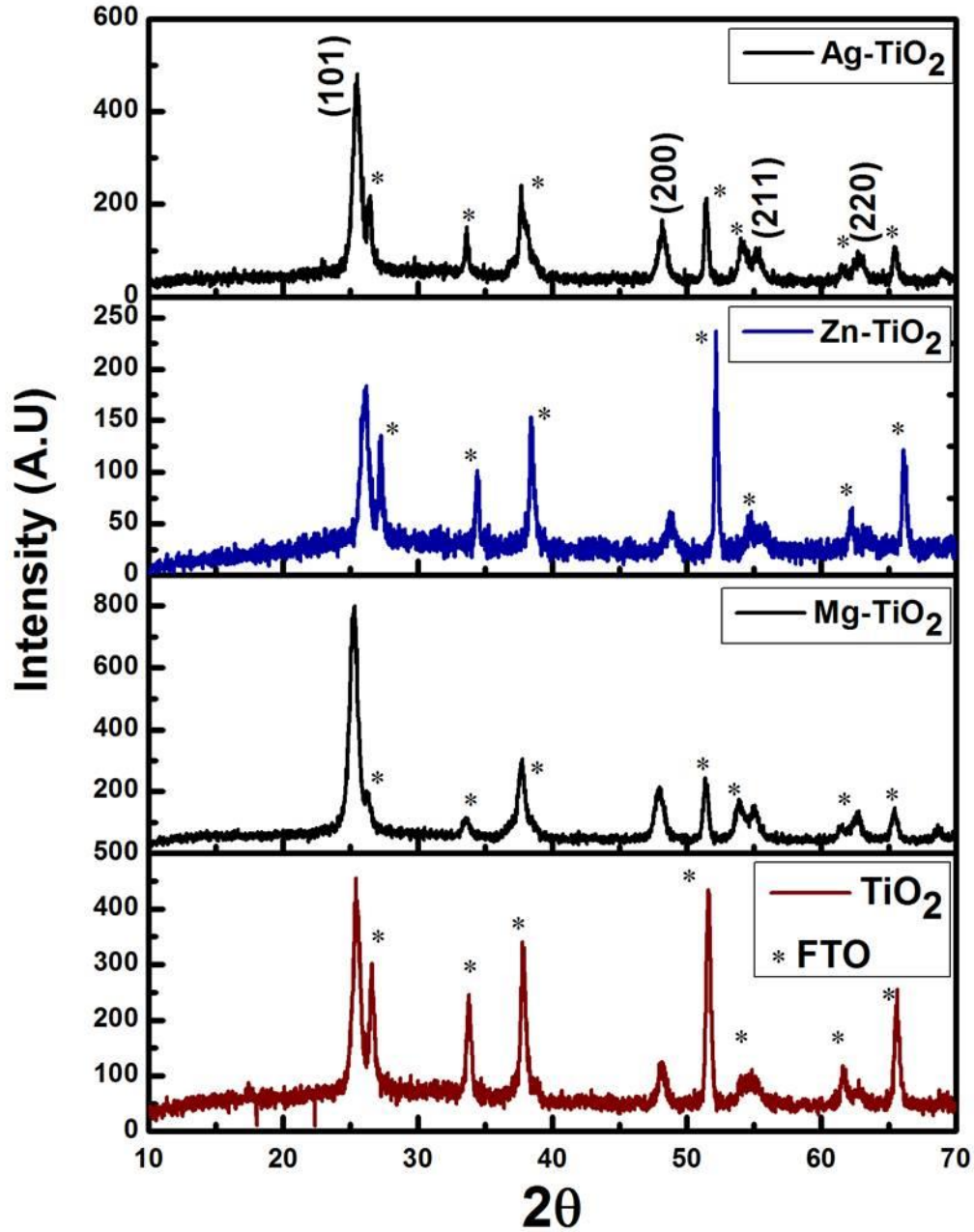


Fig. 2 XRD profile of TiO₂, Mg-TiO₂, Zn-TiO₂ and Ag-TiO₂.

To calculate the instrumental broadening, the reference material's (silicon) peak width has been calculated under similar operating conditions. The resultant full-width half maxima (FWHM) of samples were calculated by using Eq. (1)

$$\beta_D = \sqrt{\beta_{measured}^2 - \beta_{instrumental}^2} \quad (1)$$

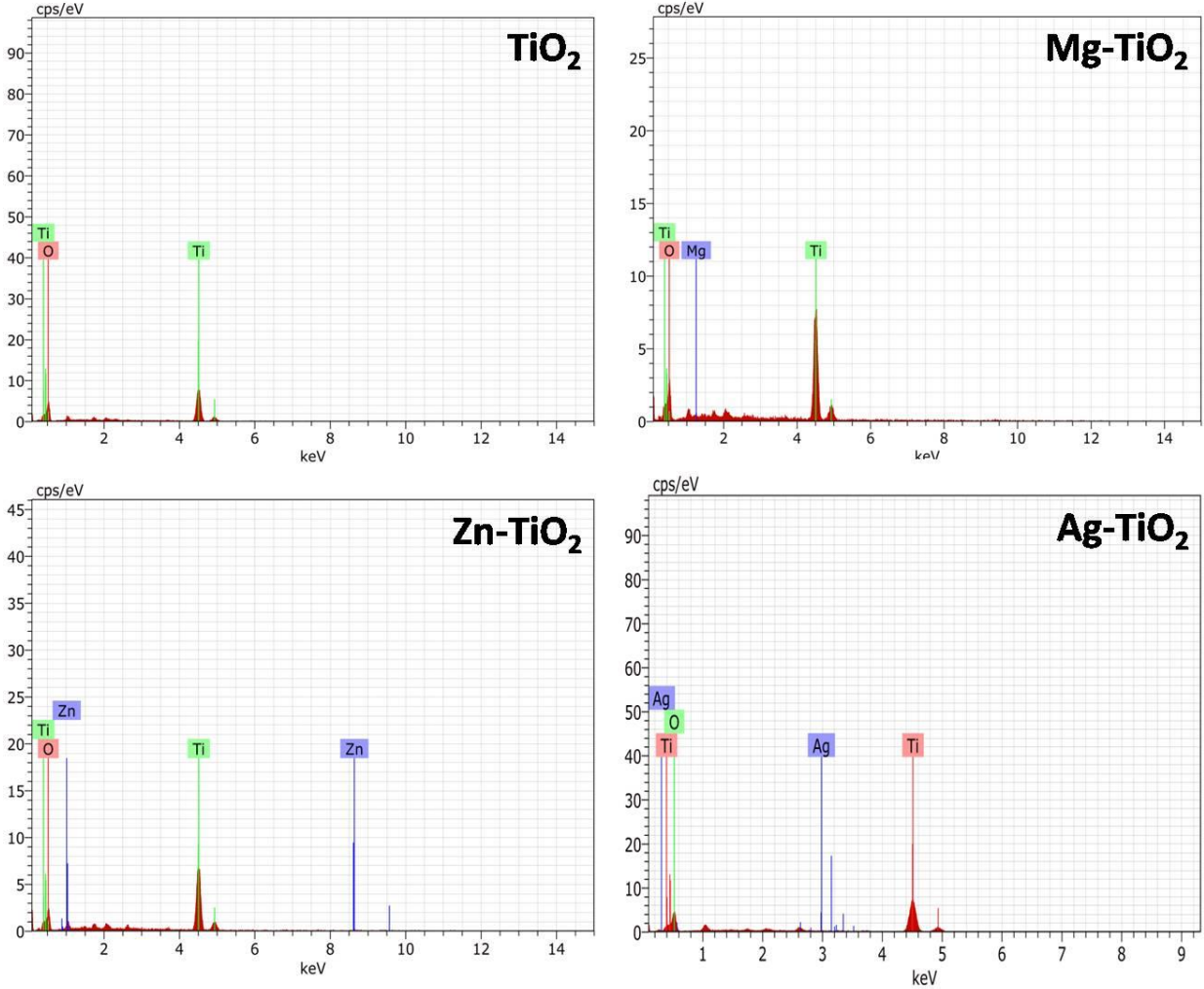


Fig. 3 EDS results of TiO₂, Mg-TiO₂, Zn-TiO₂ and Ag-TiO₂.

Where β_D is the corrected FWHM of the sample, $\beta_{measured}$ is the observed value of FWHM from diffractogram and $\beta_{instrumental}$ is FWHM because of instrumental broadening. The average value of crystallite size (D) has been found by applying Sherrer's formula [13] to the principal peak represented by (101) plane.

$$D = \frac{k\lambda}{\beta \cos\theta} \quad (2)$$

where k is the shape factor (0.9), λ is the wavelength of CuK _{α} radiation (1.54 Å), β is full-width half maxima and θ is Bragg's angle. The calculated average value of D for all the samples is tabulated in table 1. It is observed that D decreases for all the modified samples in comparison to pristine. Defects in the material produce the stress which in turn leads to rearrangement of the lattice structure. This stress induces the strain in the material which is responsible for peak broadening in XRD. The strain induced in the material is given by

$$\varepsilon = \frac{\beta_{hkl}}{4 \tan \theta} \quad (3)$$

where θ is Bragg's angle and ε is lattice strain. Eq. (2) and Eq. (3) shows that peak width varies as $1/\cos\theta$ from crystallite size and strain varies as $\tan\theta$.

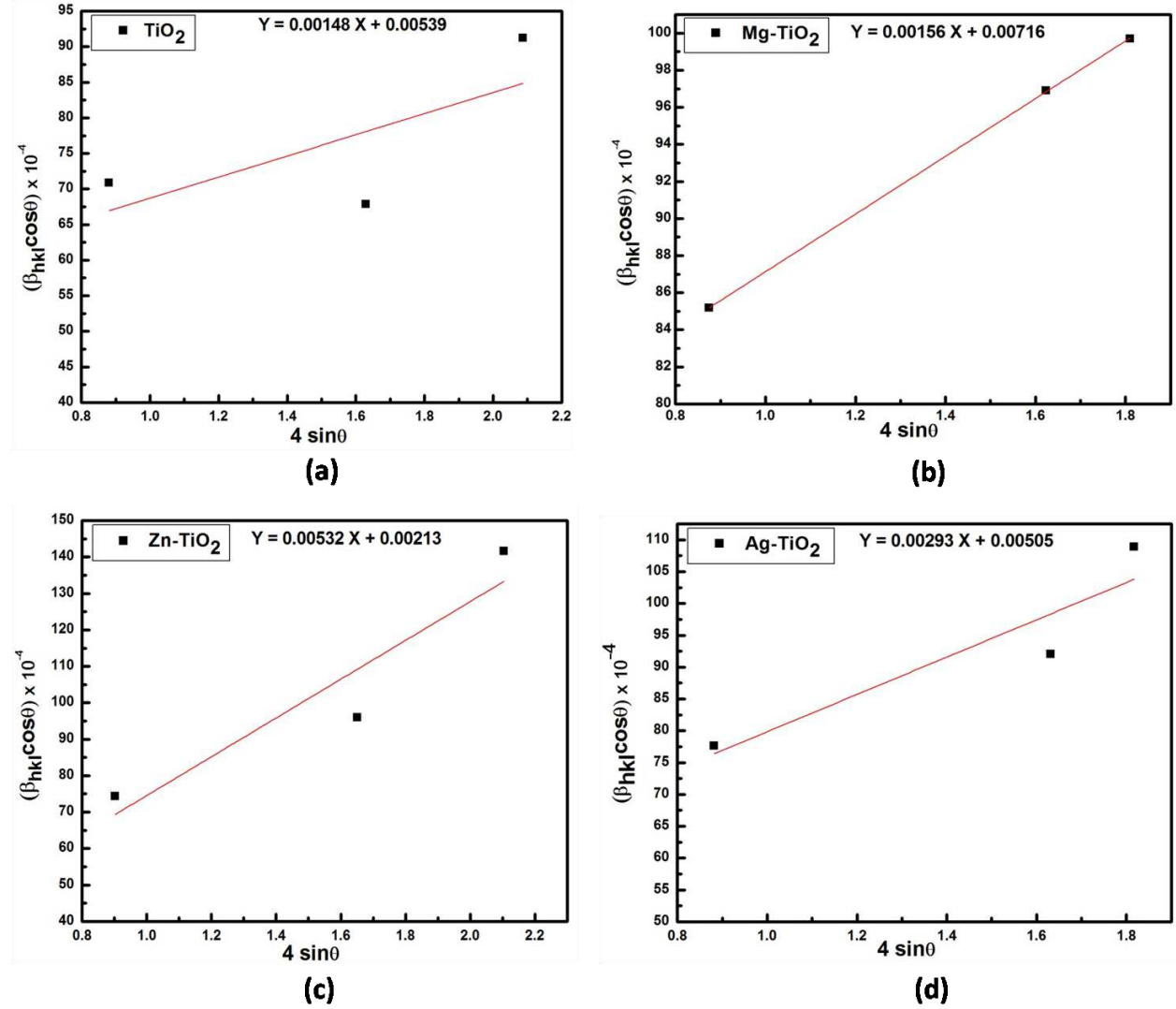


Fig. 4 $\beta_{hkl} \cos \theta$ versus $4 \sin \theta$ plots.

We assume that both strain distribution and particle size contributes independently towards the broadening of peak therefore the line breadth is the sum of Eq. (2) and Eq. (3) [13] i.e.

$$\beta_{hkl} = \frac{k\lambda}{D \cos \theta} + 4 \varepsilon \tan \theta \quad (4)$$

By rearranging Eq. (4), we get

$$\beta_{hkl} \cos \theta = \frac{k\lambda}{D} + 4 \varepsilon \sin \theta \quad (5)$$

Eq. (5) is known as Williamson's Hall (W-H) equation and it represents the Uniform Deformation Model (UDM) where the strain is assumed to be same in all crystallographic directions, thereby the isotropic nature of the crystal has been considered where the material properties are independent of the directions along which they are measured. The UDM has been applied to all the samples and the plots are shown in Fig. 4. A graph is plotted between $\beta_{hkl}\cos\theta$ along the y-axis and $4\sin\theta$ along the x-axis. A linear fit to the plot gives the intercept on the y-axis and slope to the fit. The crystallite size (D), strain (ϵ) has been calculated from the intercept and slope of W-H plots respectively. The calculated values of D and ϵ are tabulated in table 1.

Table 1. Obtained parameters, D : Crystallite size, ϵ : Strain.

Sample	D (Scherrer's method) (nm)	D (Williamson Hall method) (nm)	ϵ
TiO ₂	20	26	1.48×10^{-3}
Mg-TiO ₂	16	19	1.56×10^{-3}
Zn-TiO ₂	19	65	5.32×10^{-3}
Ag-TiO ₂	18	27	2.93×10^{-3}

From table 1, it is observed that D calculated by Scherrer's and W-H method are nearly the same for all samples except Zn-TiO₂ in which there is a significant difference in both the values. This may be due to large strain produced in it as tabulated in Table 1. The same can be interpreted from diffractogram (Fig. 2) in the manner that peaks shift is greater in Zn-TiO₂.

The optical parameters of thin films of TiO₂, Mg- TiO₂, Zn- TiO₂ and Ag-TiO₂ are studied with the help of transmittance (T) spectra in the spectral range (300 nm - 800 nm). Fig. 5(a) shows the T spectra of prepared films. It is observed that T for Mg-TiO₂, Zn-TiO₂ and Ag-TiO₂ increases as compared to pristine TiO₂ which make the visible light to pass through this layer and reach the absorber layer (perovskite) leading to the creation of carriers and hence to have an appropriate electron transport layer (ETL) material for device fabrication. From transmittance spectra, we observed that the transmittance spectrum of Ag-TiO₂ is different from other modified samples. This difference in the spectrum may be due to grain boundary scattering and also due to surface plasmon effect related to silver nanoparticles [14]. On the other side, T is related to refractive index (n) in a way, as T of the layer increases, the value of n decreases [15].

The decrease in n value predicts a decrease in density of the material and consequently decrease in refraction which tends to pass the light efficiently through the material and reach the next layer. As the refractive index dispersion is an important parameter in designing various optical devices, here we used Swanepoel's method [16, 17] to calculate it in which, the sample is assumed of non-uniform thickness deposited on a transparent substrate having refractive index value ' s '.

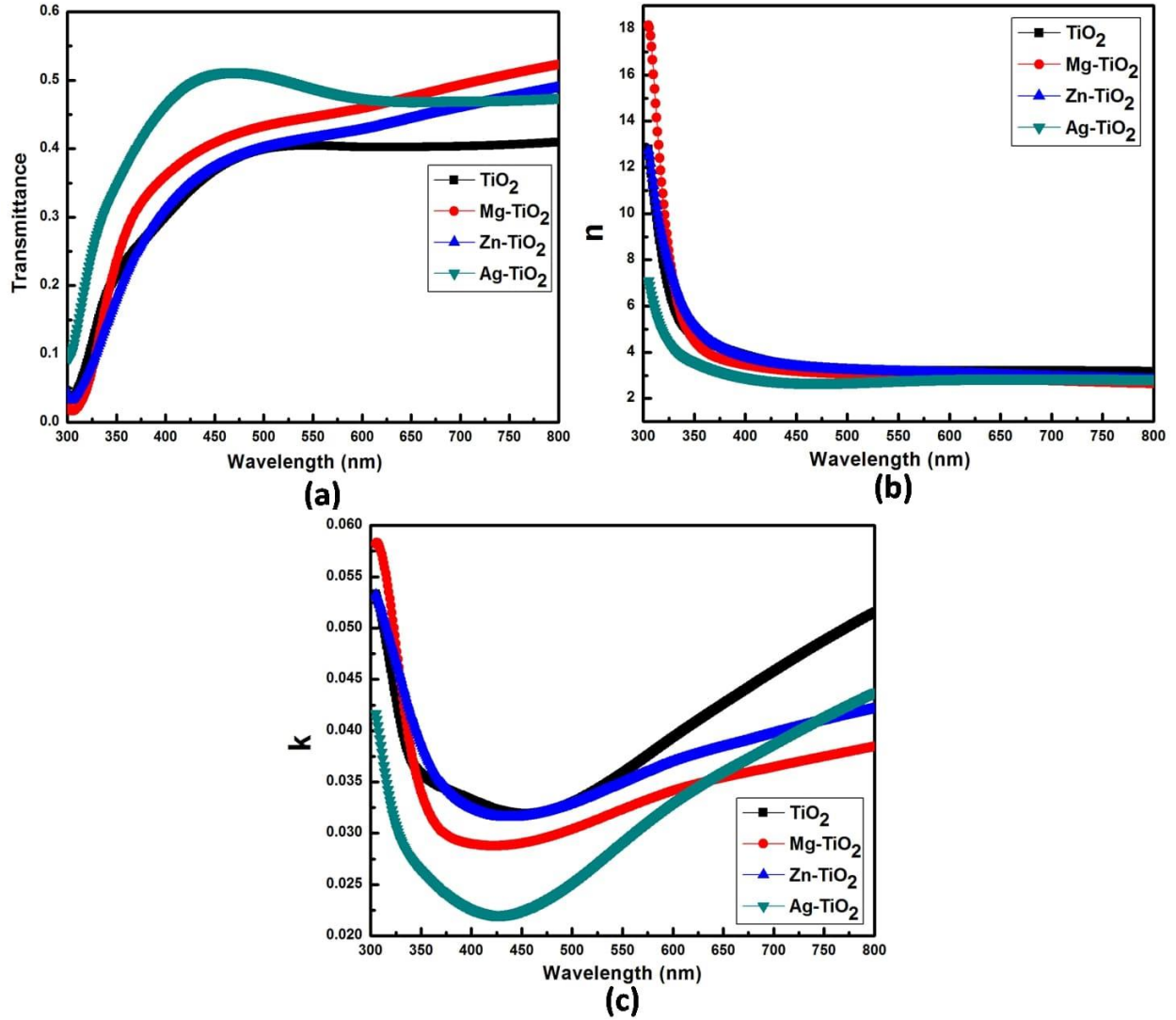


Fig. 5 (a) T versus λ variation. (b) The plot of n against λ . (c) k variation w.r.t λ .

The refractive index of the film is complex and is given by $n^* = n - ik$, where n is the refractive index and k is the extinction coefficient. This method is based upon Manifacier's approach [18] i.e in $\alpha = 0$ regions, n is calculated by Eq. 6

$$n = \sqrt{H + \sqrt{H^2 - s^2}} \quad (6)$$

Where

$$H = \frac{4s^2}{(s^2+1)T^2} - \frac{s^2+1}{2} \quad (7)$$

The calculated value of n using Eq. 6 is plotted against λ as shown in Fig. 5(b). A decrease in n with an increase of λ contributes to normal dispersion behaviour. By comparing plots of T and n with λ (Fig. 5(a), Fig. 5(b)), it is found that Ag-TiO₂ having higher T has the lowest n which is in the coordination of having decreasing n with increasing T . The imaginary part of n^* , i.e. ‘ k ’ calculated by using Eq. 8 tells us the amount of scattering and absorption per unit distance in the medium which the light propagates [19]. k shows the same trend as that of n (Fig. 5(c)) i.e. it reduces with the increment in λ .

$$k = \frac{\alpha\lambda}{4\pi} \quad (8)$$

Consequently, lesser amounts of scattering and absorption takes place which results in better transmittance and it is lowest for Ag-TiO₂. Fig. 6 shows the absorption coefficient (α) versus energy ($h\nu$) variation. It is observed that the absorption edge tail is exponential (which is shown by a blue oval in Fig. 6) for all thin films. The presence of this exponential edge indicates the presence of localized states within the bandgap. The extent of tailing can be calculated by applying first approximation to the absorption edge data in terms of an equation given by Urbach [20]. The Urbach rule is written as:

$$\alpha = \alpha_0 \exp\left(\frac{h\nu}{E_U}\right) \quad (9)$$

Where α_0 is a constant and E_U is Urbach energy which gives the exponential edge slope. There is no particular origin known for the existence of exponential dependence of α with $h\nu$ in amorphous as well as in crystalline materials. The random fluctuations of the internal fields linked with the structural disorder may be the cause of this exponential dependence [19]. E_U is nearly constant or weakly depends on temperature and often represents the width of tail of localized states in the bandgap. Lower E_U means the lower disorder in the materials.

E_U is calculated for all the samples and is given in Fig. 6. We observe that E_U value is lowest for Ag-TiO₂ suggesting the lower disorder and is highest for Zn-TiO₂ which is in agreement with XRD results. Reduction in E_U leads to a decrease in activation energy and thus decrease in the recombination of carriers which could enhance the efficiency of the ETL material [21].

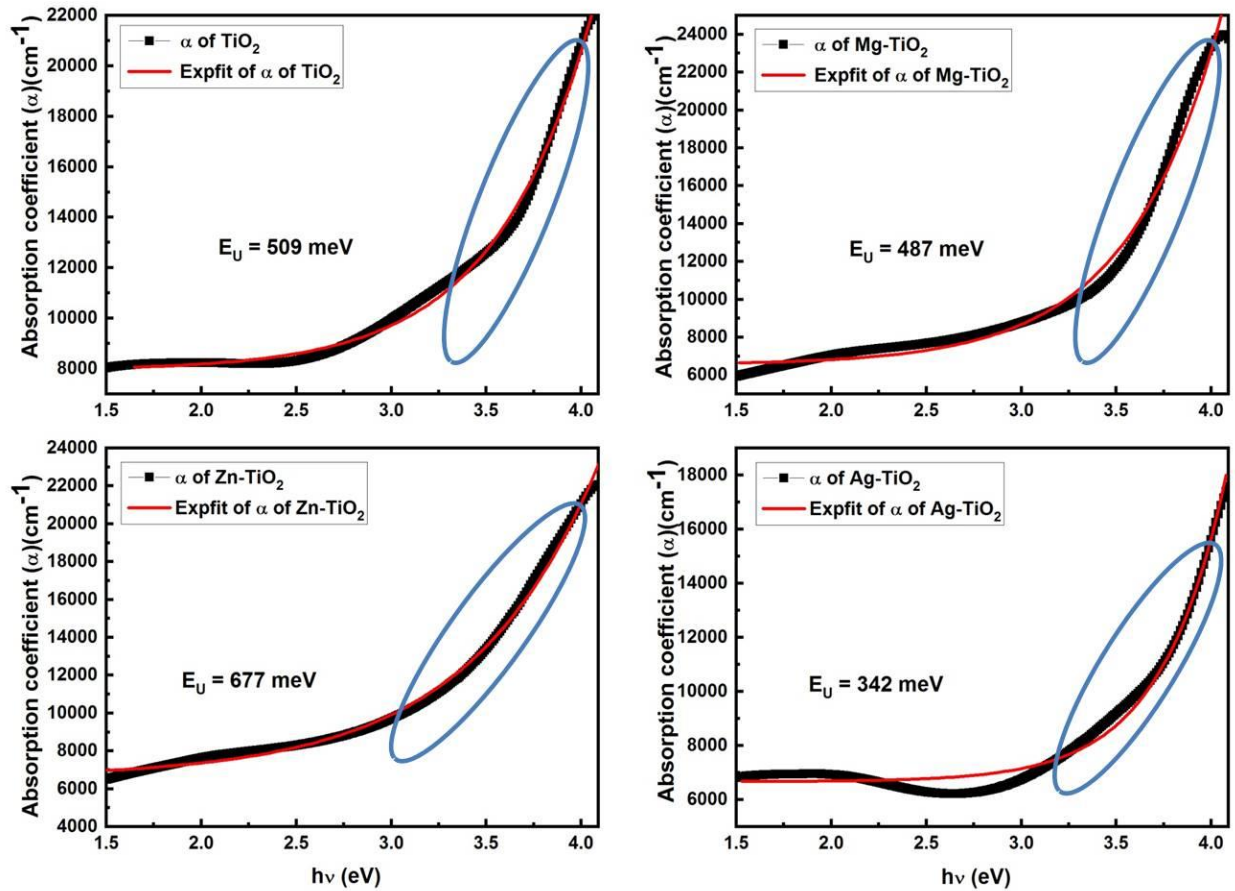


Fig. 6 Plot of α with $h\nu$.

To know the ohmic or non-ohmic nature of contacts, I-V characteristics of prepared thin films of TiO_2 , Mg-TiO_2 , Zn-TiO_2 and Ag-TiO_2 have been investigated at room temperature. The I-V plot for TiO_2 is linear with slope almost equal to unity up to the operating range of voltage (.5 V – 6 V) (as shown in Fig. 7(a)) showing ohmic nature of the contacts whereas, in other samples, the current varies non-linearly with applied voltage indicating the non-ohmic nature of contacts. This non-ohmic nature indicates that the current is increasing for doped samples as compared to pristine at the same operating voltage. This increase in current leads to enhancement in conductivity (σ) of the material [22] which is calculated at room temperature by using Eq. (10)

$$\sigma = \frac{IL}{VA} \quad (10)$$

Where ‘I’ is current, ‘L’ is the distance between the electrodes, ‘V’ is the applied voltage and ‘A’ is the area of electrodes. As given in table 2, we have calculated σ at a particular voltage of 2 volts which is found to increase from $6.08 \times 10^{-9} \Omega^{-1}\text{m}^{-1}$ for TiO_2 to $5.72 \times 10^{-8} \Omega^{-1}\text{m}^{-1}$ for Mg-TiO_2 , $6.22 \times 10^{-8} \Omega^{-1}\text{m}^{-1}$ for Zn-TiO_2 and $1.19 \times 10^{-4} \Omega^{-1}\text{m}^{-1}$ for Ag-TiO_2 which is the requirement of a good ETL in device fabrication.

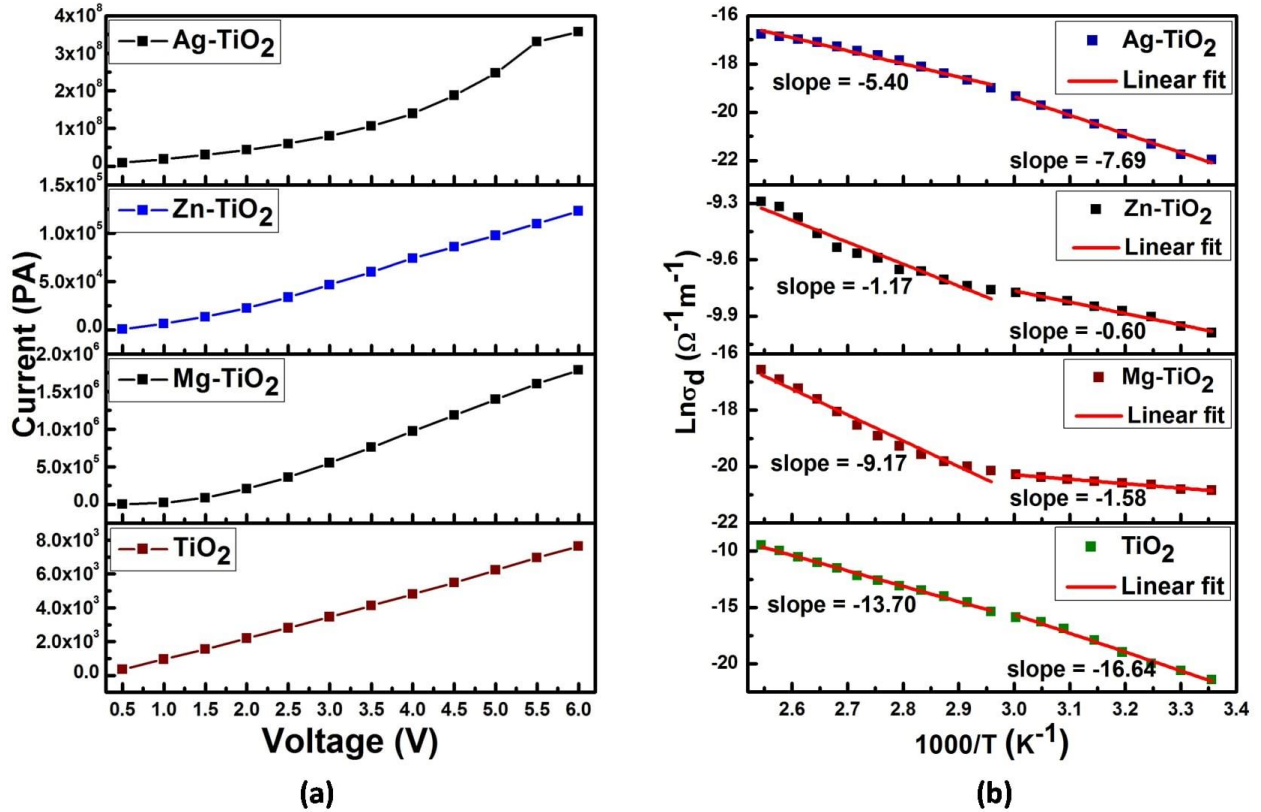


Fig. 7 (a) I-V characteristics. (b) $\text{Ln}\sigma_{\text{dc}}$ versus $1000/T$ plot in (338 K - 393 K) and (298 K - 338 K) temperature range.

To probe the current transport behaviour, temperature-dependent dark conductivity (σ_{dc}) measurements are done for all the prepared films (TiO_2 , Mg-TiO_2 , Zn-TiO_2 , Ag-TiO_2) in the temperature range (298 K - 393 K). It is found that the conductivity increases with an increase in temperature which suggests the semiconducting behaviour of the films. Based on nature of the slope, the overall temperature range (298 K - 393 K) can be divided into two regions: higher temperature region (338 K - 393 K) and intermediate temperature region (298 K - 338 K). Fig. 7(b) shows $\text{Ln}\sigma_{\text{dc}}$ versus $1000/T$ plot in two temperature regions (338 K - 393 K) and (298 K - 338 K). Therefore, σ_{dc} can be expressed as

$$\sigma_{dc} = \sigma_1 \exp\left(\frac{-\Delta E_{d1}}{kT}\right) + \sigma_2 \exp\left(\frac{-\Delta E_{d2}}{kT}\right) \quad (11)$$

Where E_{d1} , E_{d2} are activation energies in (338 K - 393 K), (298 K - 338 K) regions respectively and k is Boltzmann's constant. We have two activation energies corresponding to two regions which are tabulated in table 2.

Table 2. Obtained parameters, σ : Conductivity value at 2 Volt, E_{d1} : Activation energy in higher temperature region (338 K - 393 K), E_{d2} : Activation energy in the intermediate region (298 K - 338 K).

Material	σ ($\Omega^{-1}\text{m}^{-1}$)	E_{d1} (eV)	E_{d2} (eV)
TiO ₂	6.08×10^{-9}	1.18	1.38
Mg-TiO ₂	5.72×10^{-8}	0.79	0.14
Zn-TiO ₂	6.22×10^{-8}	0.10	0.05
Ag-TiO ₂	1.19×10^{-4}	0.46	0.67

From table 2, it is observed that E_{d1} and E_{d2} for doped samples are lower as compared to TiO₂. This decrease in activation energy as compared to pristine helps to have low recombination of charge carriers and leads to having good conductivity. The conduction in these two temperature regions can be explained based on commonly known conduction mechanisms - tunnelling [23] and thermionic emission [24]. Grain boundary trapping model can be used to explain these mechanisms as the films are polycrystalline in nature [25]. According to this model, the films have a large number of micro crystallites separated from one another by grain boundaries. Disordered atoms and partial atomic bonding between them can act as trap states. These trap states trap the free charge carriers leading to the formation of a local depletion region which acts as potential barrier tending to stop the motion of carriers from one crystallite to other. The carriers which have sufficient energy at the grain boundary to surmount this potential barrier leads to thermionic emission. On the other side, the tunnelling occurs for those carriers which do not have enough energy to cross this energy barrier [23, 25]. The high E_{d1} indicates the presence of thermionic emission as the dominant conduction mechanism in this region. On the other hand, the Arrhenius plot in the intermediate temperature region in which all E_{d2} values are found

greater than kT gives the thermionic emission as one of the conduction mechanism in this region. Since the temperature range and E_{d2} values are too high to observe hopping so tunnelling has been observed in this region.

Dielectric studies involve the participation of dielectric constant (ϵ') which is one of the basic parameter giving information about atoms, ions and polarization mechanism. This approach helps us to have the real and imaginary part of the electrical parameters and thus gives information about the properties of the material. As TiO_2 exists in three phases (anatase, brookite and rutile), anatase phase has been preferred for its dielectric properties. It has been of great interest for applications in the telecommunications industry due to its unusual high dielectric constant and low dielectric loss. The main difficulty encountered with TiO_2 is the high recombination rate of photoexcited electron-hole pairs in the irradiated particles. To deal with this problem, a generic way is to modify TiO_2 by doping with suitable material. The study of dielectric behaviour of pristine TiO_2 and $Mg-TiO_2$, $Zn-TiO_2$ and $Ag-TiO_2$ has been done over a range of 50 Hz - 5 MHz. The parameters, dielectric constant (ϵ') and dielectric loss (ϵ'') have been calculated by using Eq. 12 and Eq. 13 respectively [26].

$$\epsilon' = \frac{cd}{\epsilon_0 A} \quad (12)$$

$$\epsilon'' = \frac{Gd}{2\pi f \epsilon_0 A} \quad (13)$$

Where C , d , A , G , f and ϵ_0 are the measured capacitance, the thickness of the film, area of electrodes, conductance, applied frequency and dielectric constant in a vacuum ($8.85 \times 10^{-12} \text{ Fm}^{-1}$) respectively. The cross-section of the film is shown in Fig. 8 to have the thickness of the film.

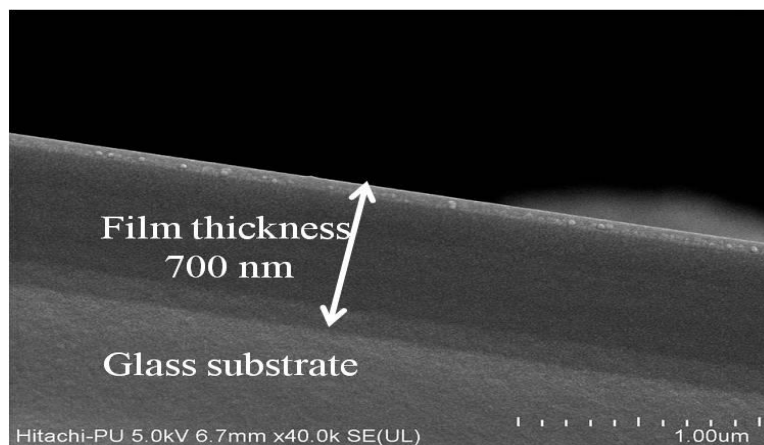


Fig. 8 Cross-section of the film.

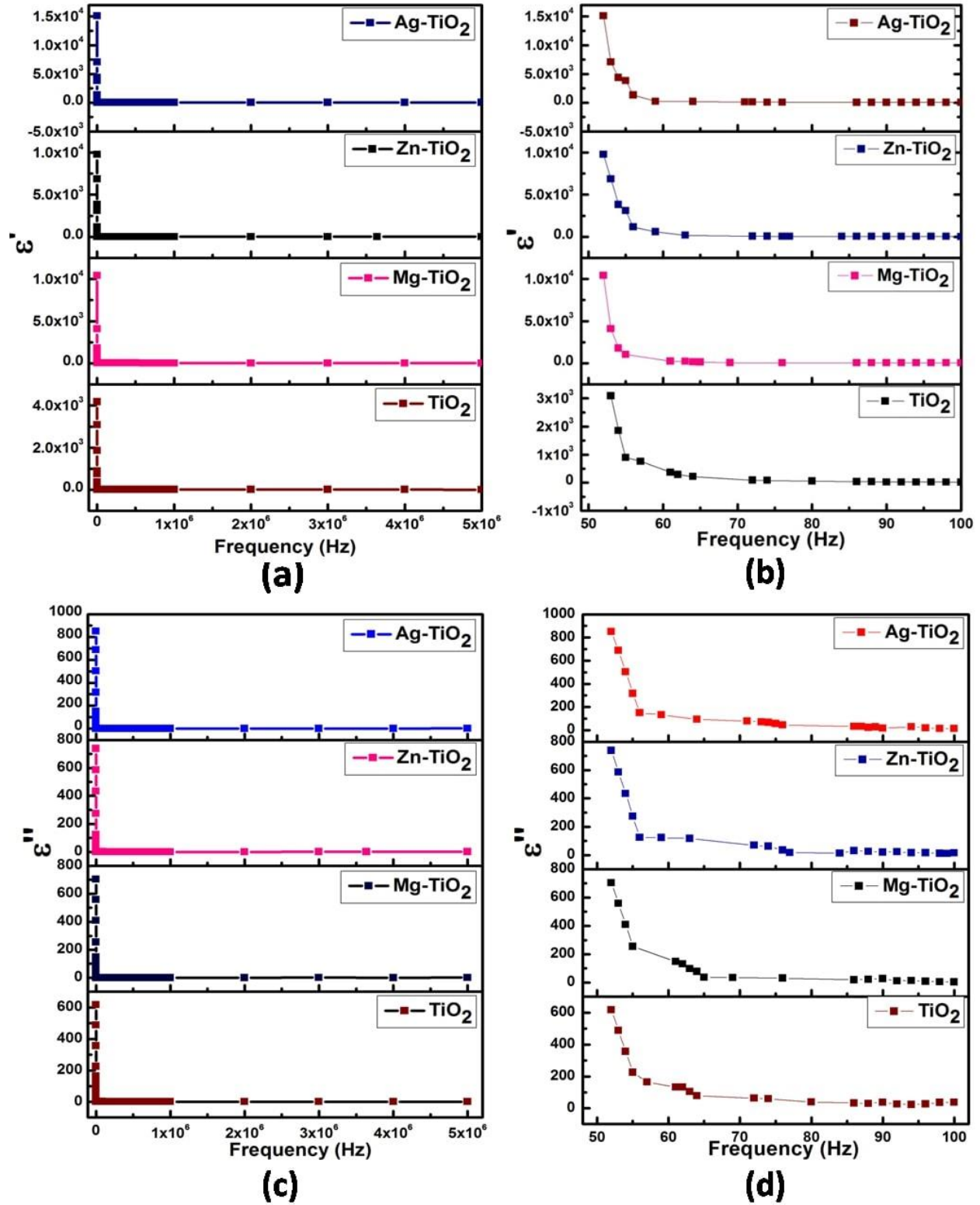


Fig. 8 (a) ϵ' versus frequency variation (50 Hz - 5 MHz). (b) ϵ'' versus frequency variation. (c) ϵ' versus frequency variation (50 Hz - 5 MHz). (d) ϵ'' versus frequency variation.

The variation of the real and imaginary part of the dielectric constant i.e. (ϵ' and ϵ'') as a function of frequency (50 Hz -5 MHz) at room temperature are shown in Fig. 9(a) and Fig. 9(c). It is observed that ϵ' value is higher at low frequencies shown separately also in Fig. 9(b) and it decreases with the increase in frequency. The relation of ϵ' with binding energy (E_b) of carriers is given by using Eq. 14 [27]

$$E_b = \frac{\mu e^2}{2h^2 \epsilon'^2} \quad (14)$$

Where μ is the effective mass of electron and e is the charge on the electron. One may notice that ϵ' goes on increasing for doped samples as compared to pristine one (Fig. 9(a), (b)) which leads to a reduction in E_b of the charge carriers and hence enhancement in their separation takes place leading to increased movement of charge carriers. This result is in good agreement with our I-V results as the conductivity follows the same order as the dielectric constant ($\text{Ag-TiO}_2 > \text{Zn-TiO}_2 > \text{Mg-TiO}_2 > \text{TiO}_2$). High ϵ' suggests the presence of space charge orientation, ionic and electronic polarization. The same trend has been observed for ϵ'' versus frequency (f) plots (Fig. 9(c)). ϵ'' versus frequency (f) for low-frequency range is also shown in Fig. 9(d). ϵ' versus ' f ' variation can be explained based on Maxwell-Wagner and Koops phenomenological theory [28, 29].

According to this model, there are several well-distributed conducting grains separated by partially conducting grain boundaries. There is a great effect on these grains at higher frequencies whereas at low frequencies it is the grain boundaries that play a major role. At low frequency, the dielectric constant is due to the accumulation of charge carriers under the application of electric field which in turn leads to surface charge polarization. As the frequency changes, the field changes at a very fast rate which makes it difficult for the electrons to keep them in pace with the field and hence they lag behind the applied field due to slow movement of electrons with the changing field. This lagging of electrons spread over the whole area and ultimately reaches to grain boundaries which lead to a decrease in ϵ' with an increase in ' f '. The cause of a decrease in ϵ' can be explained based on polarization also. The polarization of material is the contribution of ionic, electronic, dipolar and interfacial polarization. The dielectric behaviour of the material is divided into two regions: (a) variation of ϵ' at high frequency. (b) variation of ϵ' at low frequency. The high value of ϵ' at a low value of frequency is because of the good response of polarization (especially surface charge polarization) with the varying field. In the reverse of it, a low value of ϵ' is due to the poor response of polarization with the applied

field. In addition to it, the charge carriers fail to go in coordination with the field at high frequencies which leads to a decrease in ϵ' . Also, there are impurities, defect states and space charge formation between different interface layers of nanomaterials which results in the production of absorption current leading to dielectric loss (ϵ''). ϵ'' decreases with the increase in frequency due to the decrease in absorption current. However, charge movement conversion to lattice vibration i.e. photon causes the ϵ'' at high-frequency [30, 31].

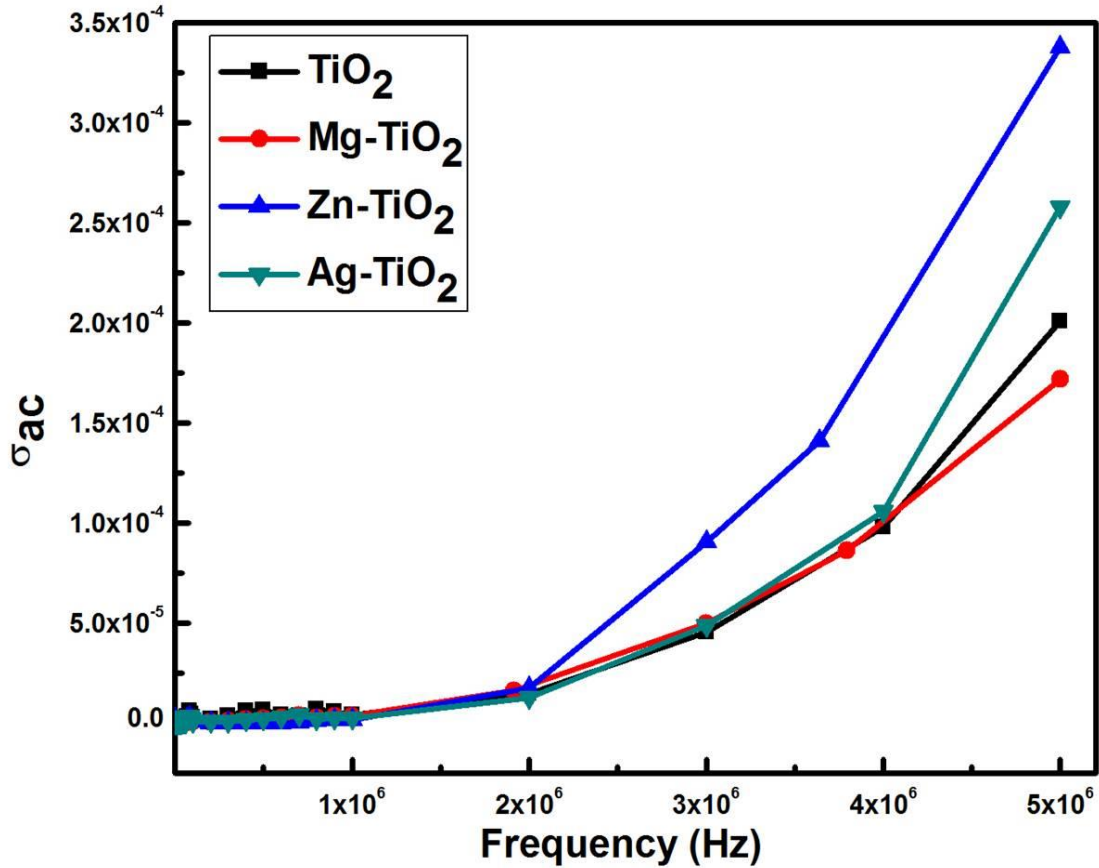


Fig. 10 σ_{ac} versus 'f' plot.

The ac conductivity (σ_{ac}) has been calculated by using Eq. 15

$$\sigma_{ac} = \epsilon'' \epsilon_0 2\pi f \quad (15)$$

Fig. 10 shows the frequency dependence of σ_{ac} for all the samples. AC conductivity possesses low value in the low-frequency region whereas it starts increasing in the high-frequency region. The value of σ_{ac} is higher for doped samples than the pristine one. Zn-TiO₂ has higher σ_{ac} followed by Ag-TiO₂ and Mg-TiO₂. This increase in σ_{ac} value helps the researchers to use these

materials in various applications to have enhanced conductivity. At low frequency, the low value of σ_{ac} is due to surface charge polarization whereas, at high frequency, high σ_{ac} value is due to hopping phenomenon [32, 33].

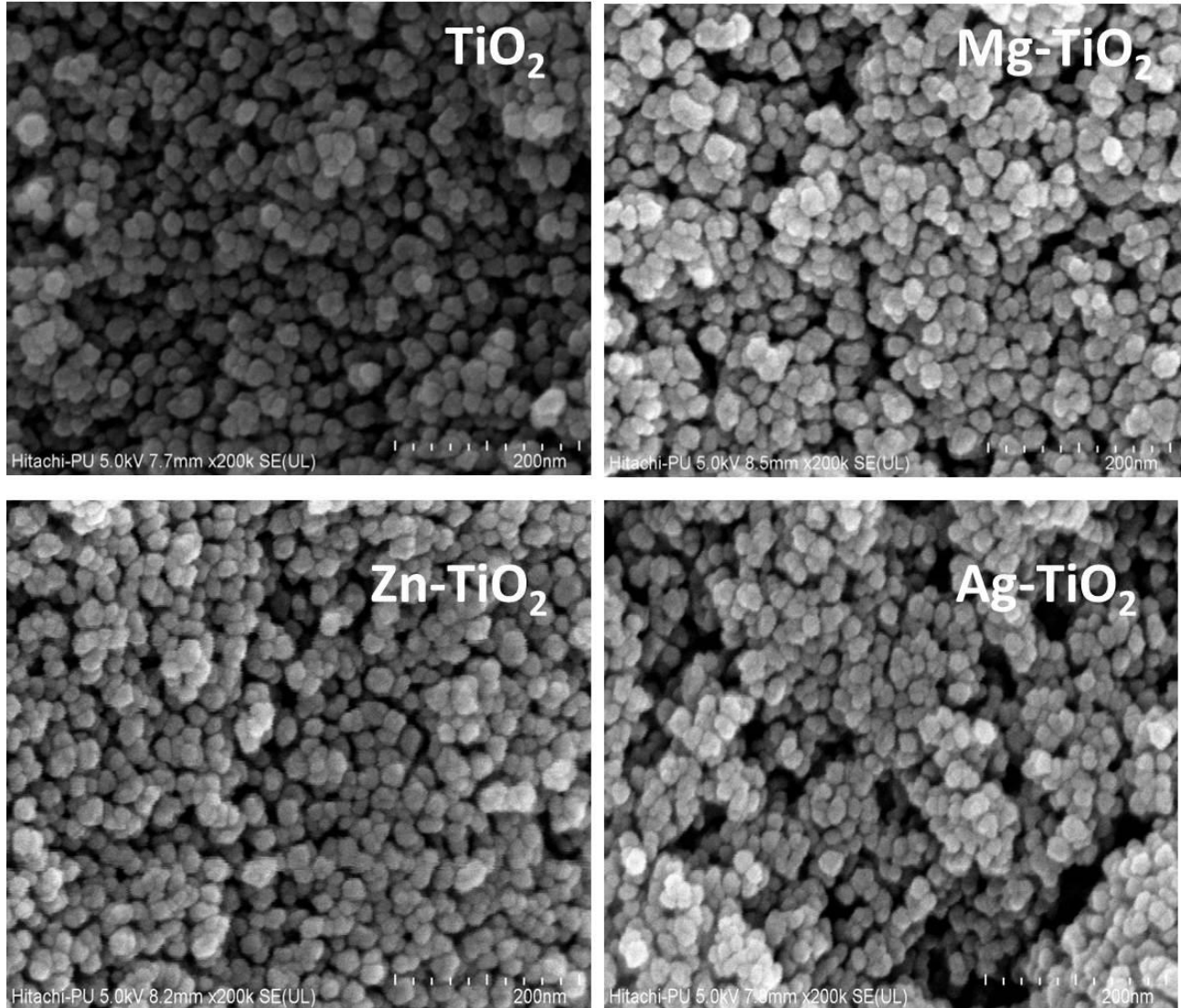


Fig. 11 Surface morphology of TiO₂, Mg- TiO₂, Zn- TiO₂ and Ag- TiO₂.

Fig.11 shows the morphology of the spin-coated compact and mesoporous layer. It represents the spherical shape of the particles in all the samples having some pores inside them. These pores are higher in modified samples as compared to pristine TiO₂ and help the carriers to move efficiently which ultimately enhance the conductivity of the carriers. This result is in good agreement with the I-V results which shows the enhancement of current in modified samples and also in dielectric studies which gives the decrease in the binding energy of carriers. To investigate the photovoltaic performance of prepared devices, current-voltage (I-V) characteristics are measured

under simulated (1000W/m^2) irradiation by using Wavelabs LED Solar Simulator SINUS 70 as shown in Fig. 12 and the characterization is repeated to become sure about the obtained results.

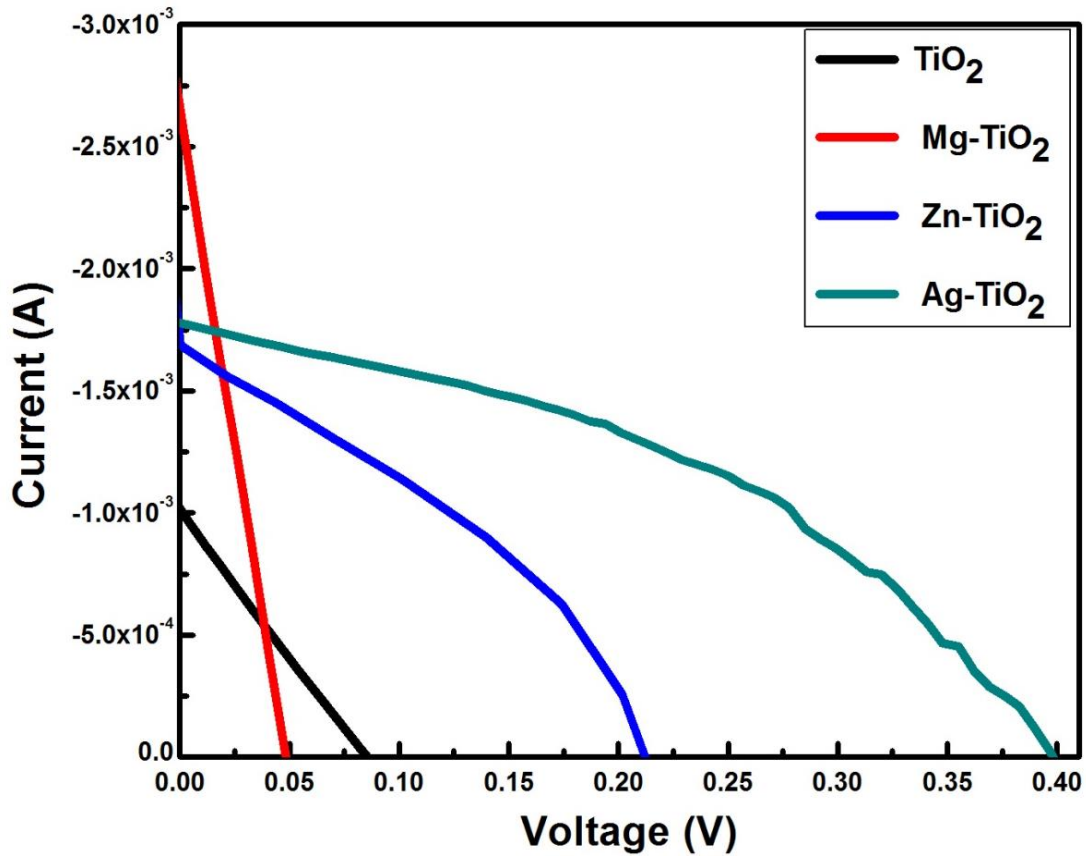


Fig. 12 I-V plots of device (a), (b), (c) and (d).

Photovoltaic parameters of all the four devices (FTO/TiO₂/CH₃NH₃PbI₃/CuSCN/Au)(a), (FTO/Mg-TiO₂/CH₃NH₃PbI₃/CuSCN/Au)(b), (FTO/Zn-TiO₂/CH₃NH₃PbI₃/CuSCN/Au)(c) and (FTO/Ag-TiO₂/CH₃NH₃PbI₃/CuSCN/Au)(d) are tabulated in table 3. The best device according to our results shows the power conversion efficiency (PCE) of 1.8%, open-circuit voltage (V_{oc}) of 0.39 V and short circuit current (I_{sc}) of 1.78 mA. From table 3, we observed that PCE order of device is device(d)(1.8%) > device(c)(1.1%) > device(b)(0.9%) > device(a)(0.5%). The device characterization results are also in good agreement with the other characterizations (structural, optical, electrical and dielectric). Doping in the pristine material modified the required parameters in the desired manner. The low efficiency of the devices may be due to less uniformity of the films and the low matched interface between the different layers.

Table 3. Obtained parameters: V_{oc} : Open circuit voltage, I_{sc} : Short circuit current, PCE: Power conversion efficiency.

Device	V_{oc}	I_{sc} (mA)	PCE(%)
FTO/TiO ₂ /CH ₃ NH ₃ PbI ₃ /CuSCN/Au	0.08	1.01	0.5
FTO/Mg-TiO ₂ /CH ₃ NH ₃ PbI ₃ /CuSCN/Au	0.04	2.70	0.9
FTO/Zn-TiO ₂ /CH ₃ NH ₃ PbI ₃ /CuSCN/Au	0.21	1.68	1.1
FTO/Ag-TiO ₂ /CH ₃ NH ₃ PbI ₃ /CuSCN/Au	0.39	1.78	1.8

8. Conclusion

In this work, researchers have modified the properties of TiO₂ by employing doping of Mg, Zn and Ag. Addition of the dopants leads to an increase of current in the pristine material which in turn enhance the conductivity in the order Ag-TiO₂>Zn-TiO₂>Mg-TiO₂>TiO₂. Dielectric studies reveal the fact that dielectric constant increase with doping. This enhancement in dielectric constant causes the decrease in the binding energy of the carriers enabling the easy movement of charge carriers. The modified nanoparticles have been utilized as mesoporous ETL in device fabrication (PSCs) gives the high power conversion efficiency as compared to pristine which makes this doping work successful.

Acknowledgements This work is financially supported by UGC-CAS, New Delhi. Authors would like to thank Dr. Sushobhan Avasthi for providing solar simulator. Also, Ms. Nazilla Soleimanioun is thankful to the Indian Council for Cultural Relations (ICCR) for granting the scholarship.

Author contributions: Sameeksha Sharma and Nazilla Soleimanioun have carried out experimental findings of this work. Prof. S.K. Tripathi and Dr. Mamta Rani supervised the findings of this work. All authors discussed the results and contributed to the final manuscript.

Conflict of interest

The authors declare that they have no known competing financial interests or personal relationships that could have appeared to influence the work reported in this paper.

References

1. R. L. Z. Hoye, K. P. Musselman, J. L. MacManus-Driscoll, *APL Mater.* 1(6), 060701 (2013).
2. S. Abdellatif, P. Sharifi, K. Kirah, R. Ghannam, A. S. G. Khalil, D. Erni, F. Marlow, *Microporous Mesoporous Mater.* 264, 84 (2018).
3. C. J. Tavares, S. M. Marques, L. Rebouta, S. Lanceros-Méndez, V. Sencadas, C. M. Costa, E. Alves, A. J. Fernandes, *Thin Solid Films* 517, 1161 (2008).
4. J. Shi, X. Wang, *Cryst. Growth Des.* 11, 949 (2011).
5. B. Roose, S. Pathak, U. Steiner, *Chem. Soc. Rev.* 44, 8326 (2015).
6. C. Stella, D. Prabhakar, N. Soundararajan, K. Ramachandran, *AIP Conference Proceedings* 1731, 050020 (2016).
7. J. Zhu, J. Zhang, F. Chen, K. Iino, M. Anpo, *Topics in Catalysis* 35, 261 (2005).
8. H. S. Kim, C. R. Lee, J. H. Im, K. B. Lee, T. Moehl, A. Marchioro, S. J. Moon, R. H. Baker, J. H. Yum, J. E. Moser, M. Grätzel, N. G. Park, *Sci. Rep.* 2, 591 (2012).
9. K. M. Prabu, P. M. Anbarasan, *IJSR* 3, 132 (2014).
10. M. R. Ahmadian-Yazdi, M. Habibi, M. Eslamian, *Appl. Sci.* 8, 308 (2018).
11. Z. L. Zhang, J. F. Li, X. L. Wang, J. Q. Qin, W. J. Shi, Y. F. Liu, H. P. Gao, Y. L. Mao, *Nanoscale Res. Lett.* 12, 43 (2017).
12. N. Kumar, G. K. Sidhu, R. Kumar, *Mater. Res. Express* 6, 075019 (2019).
13. V. D. Mote, Y. Purushotham, B. N. Dole, *Journal of Theoretical and Applied Physics* 6, 6 (2012).
14. H. Sutanto, S. Wibowo, I. Nurhasanah, E. Hidayanto, H. Hadiyanto, *Int. J. Chem. Eng.* Volume 2016, Article ID 6195326, 6 pages. <http://dx.doi.org/10.1155/2016/6195326>.
15. K. H. Abass, *International Letters of Chemistry, Physics and Astronomy* 45, 24 (2015).
16. R. Swanepoel, *J. Phys. E: Sci. Instrum.* 16, 1214 (1983).
17. R. Swanepoel, *J. Phys. E: Sci. Instrum.* 17, 896 (1984).
18. J. C. Manifacier, J. Gasiot, J. P. Fillard, *J. Phys. E: Sci. Instrum.* 9, 1002 (1976).
19. K. Sharma, A. S. Al-Kabbi, G. S. S. Saini, S. K. Tripathi, *Mater. Res. Bull.* 47, 1400 (2012).
20. J. M. González-Leal, E. Márquez, A. M. Bernal-Oliva, J. J. Ruiz-Pérez, R. Jimenez-Garay, *Thin Solid Films* 317, 223 (1998).

21. M. Abdi-Jalebi, M. I. Dar, A. Sadhanala, S. P. Senanayak, F. Giordano, S. M. Zakeeruddin, M. Grätzel, R. H. Friend, *J. Phys. Chem. Lett.* 7, 3264 (2016).
22. N. Soleimanioun, M. Rani, S. Sharma, A. Kumar, S. K. Tripathi, *Sol. Energy Mater. Sol. Cells* 191, 339 (2019).
23. M. V. Garcia-Cuenca, J. L. Morenza, J. Esteve, *J. Appl. Phys.* 56, 1738 (1984).
24. J. Y. W. Seto, *J. Appl. Phys.* 46, 5247 (1975).
25. G. Baccarani, B. Riccà, G. Spadini, *J. Appl. Phys.* 49, 5565 (1978).
26. Poonam, K. Sharma, N. Singh, S. K. Tripathi, *Mater. Res. Express* 6, 025502 (2019).
27. M. D. Sturg, *Phy. Rev.* 127, 768 (1962).
28. S. Saafan, S. Assar, S. Mansour, *J. Alloy Compd.* 542, 192 (2012).
29. R. Nongjai, S. Khan, K. Asokan, H. Ahmed, I. Khan, *J. Appl. Phys.* 112, 084321 (2012).
30. J. Hassan , F. M. Yen, M. Hashim, Z. Abbas, Z. A. Wahab, W. M. D. W. Yusoff, A. Zakaria, *Ionics* 13, 219 (2007).
31. K. P. Priyanka, S. Joseph, S. Thankachan, E. M. Mohammed, T. Varghese, *J. Basic Appl. Sci.* 2, 105 (2013).
32. V. Biju, M. A. Khadar, *J. Mater. Sci. Lett.* 36, 5779 (2001).
33. D. P. Snowden, H. Saltsburg, *Phys. Rev. Lett.* 14, 497 (1965).

Figures

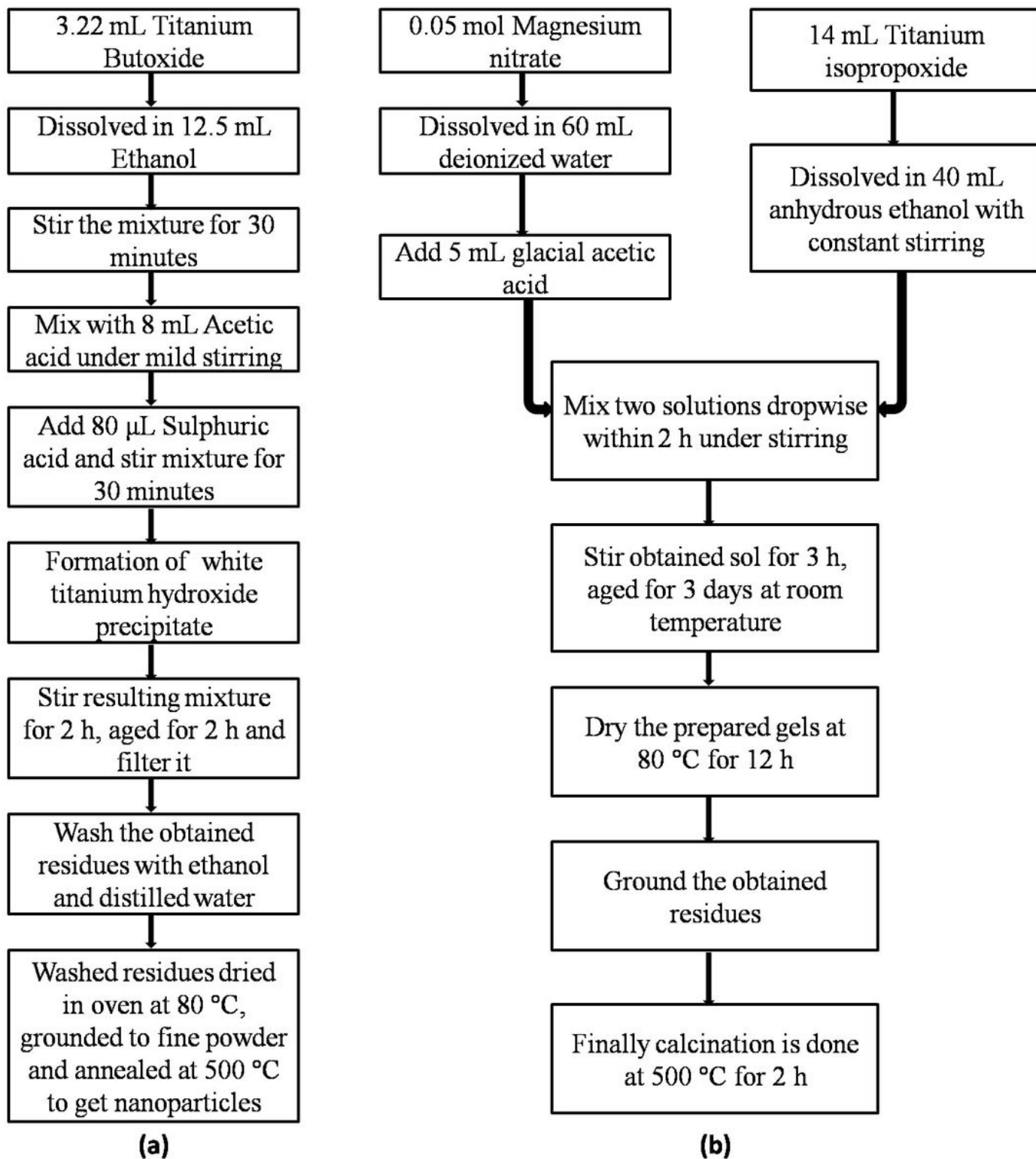


Figure 1

Synthesis procedure for (a) TiO₂ nanoparticles. (b) doped TiO₂ nanoparticles.

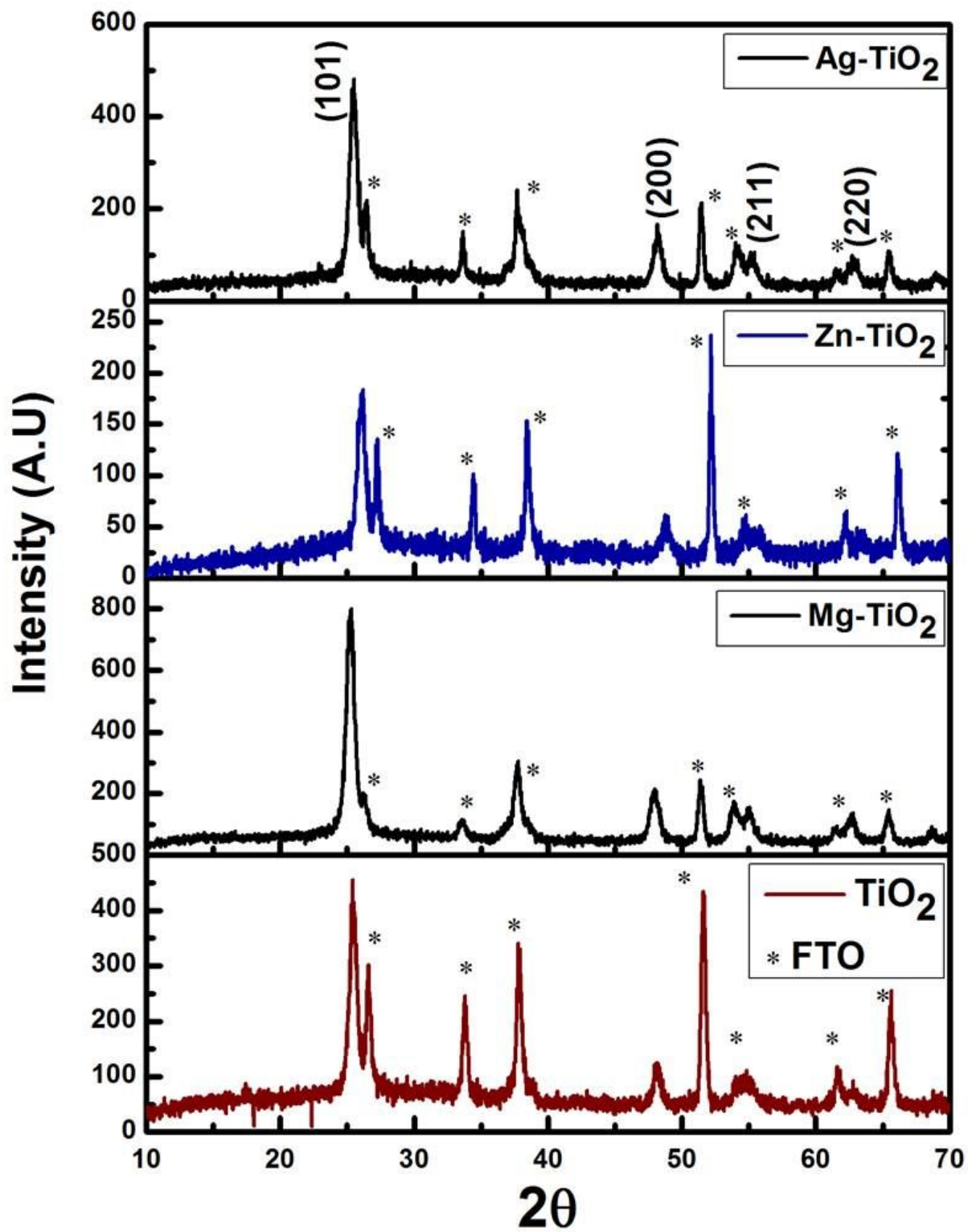


Figure 2

XRD profile of TiO₂, Mg-TiO₂, Zn-TiO₂ and Ag-TiO₂.

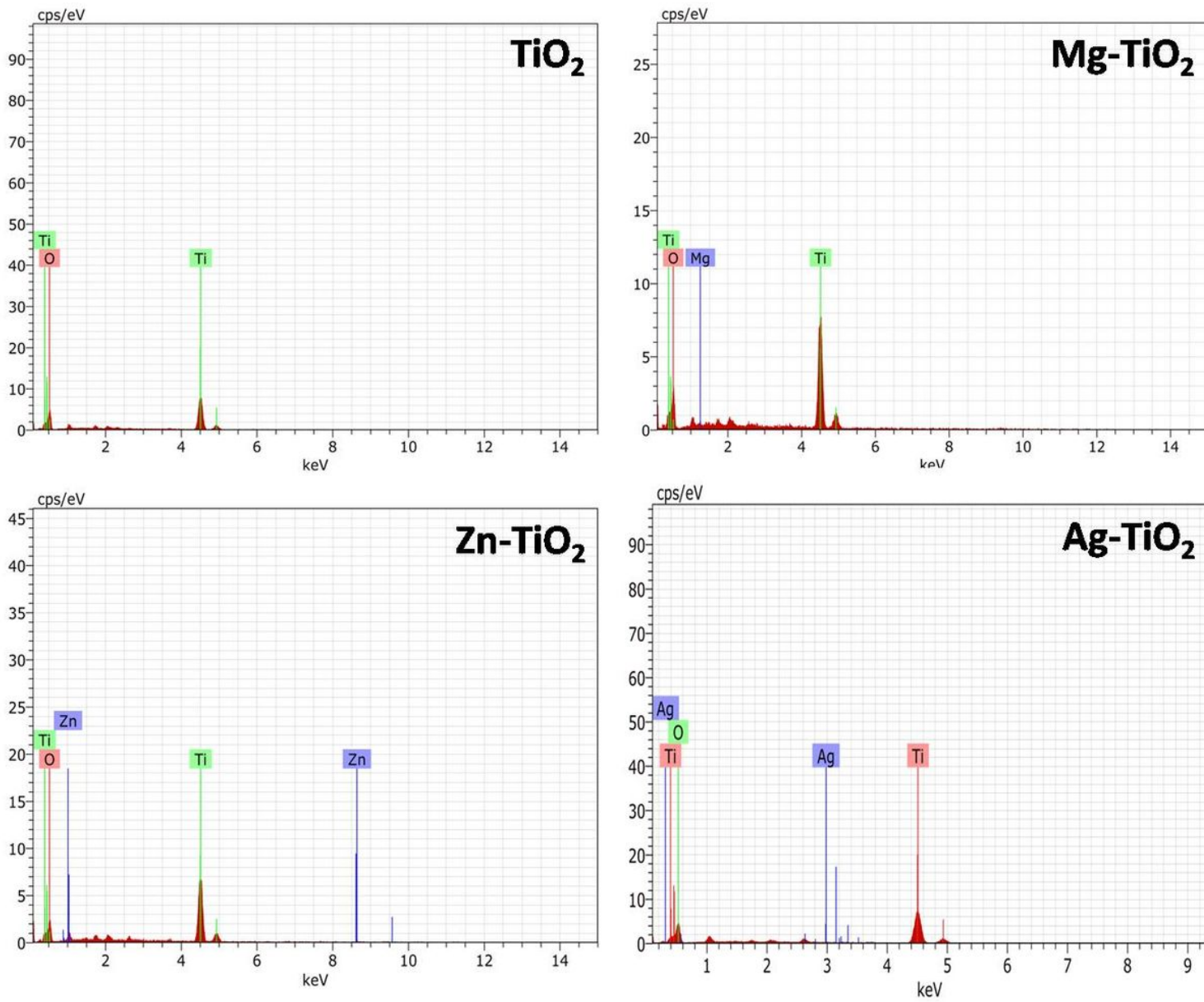
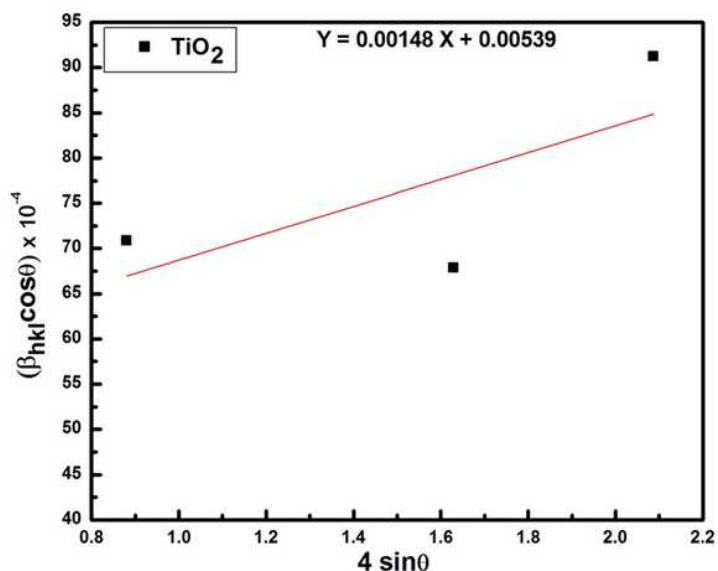
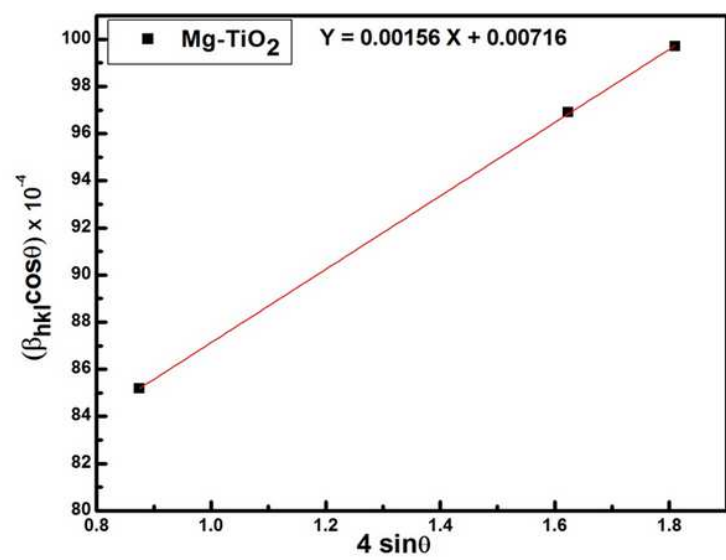


Figure 3

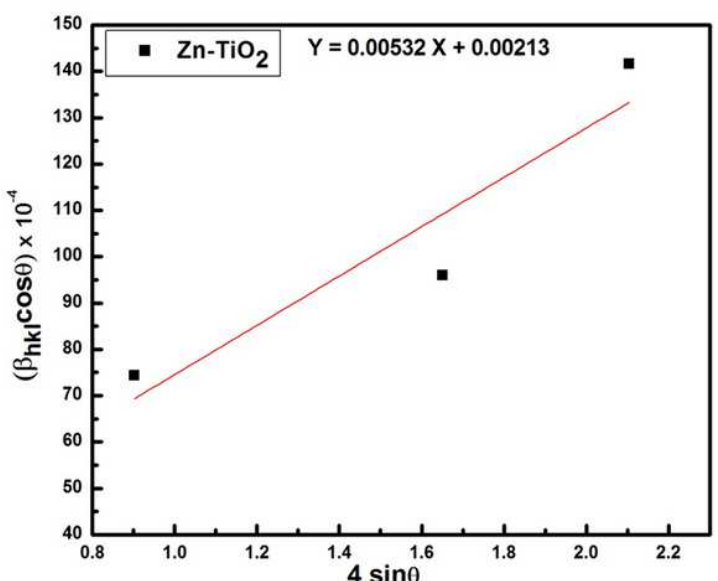
EDS results of TiO₂, Mg-TiO₂, Zn-TiO₂ and Ag-TiO₂.



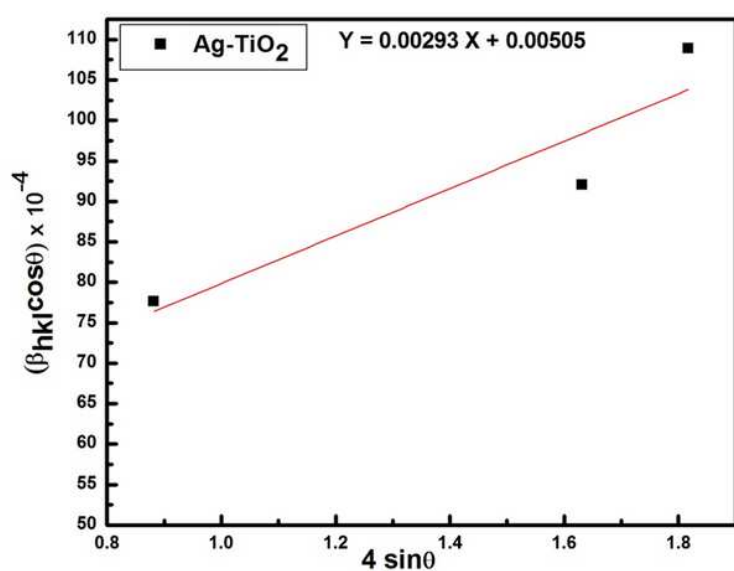
(a)



(b)



(c)



(d)

Figure 4

Please see the Manuscript PDF file for the complete figure caption

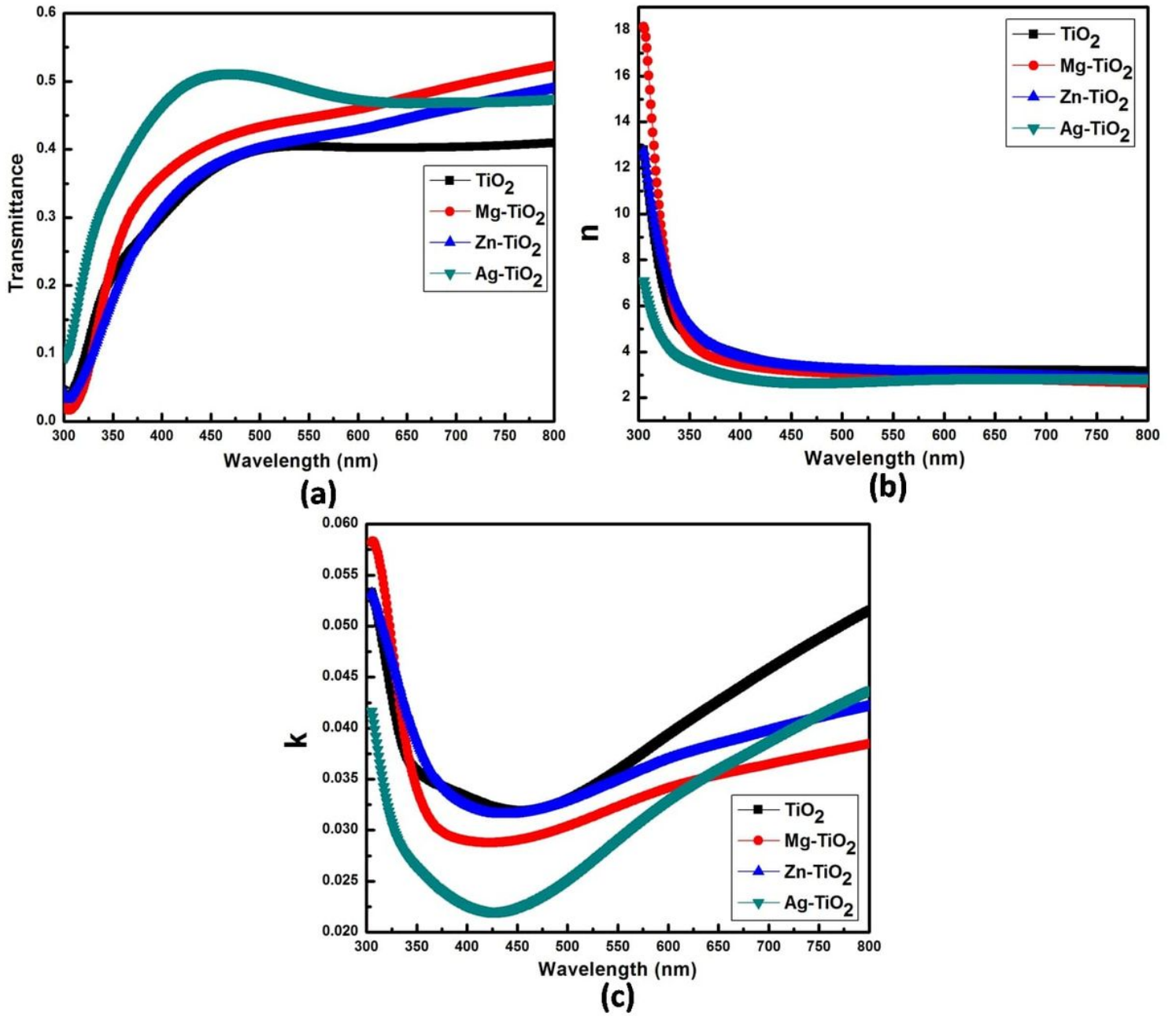


Figure 5

(a) T versus λ variation. (b) The plot of n against λ . (c) k variation w.r.t λ .

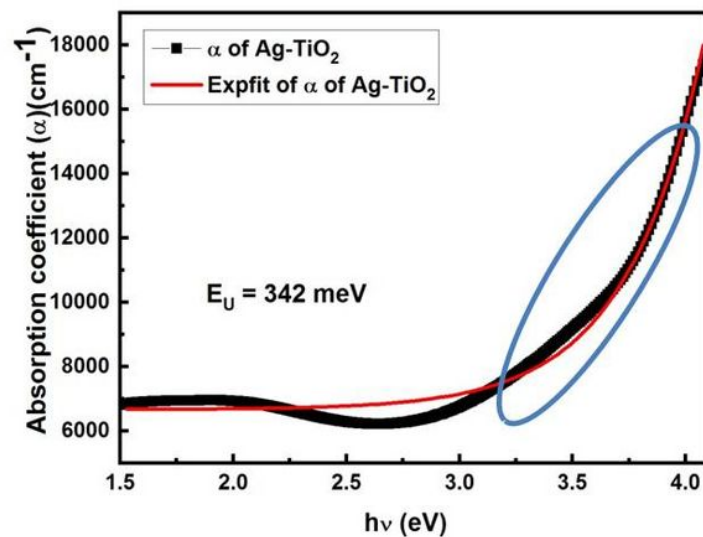
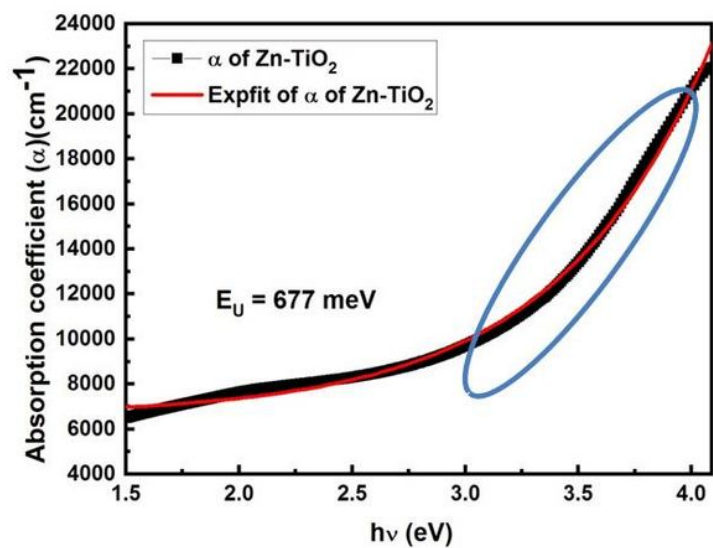
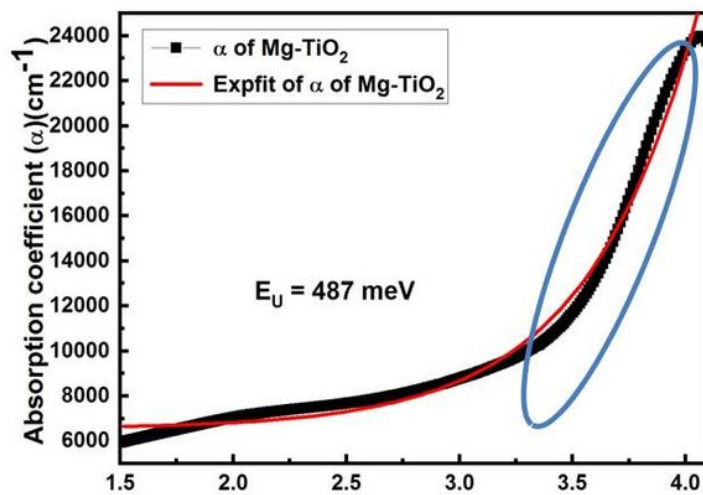
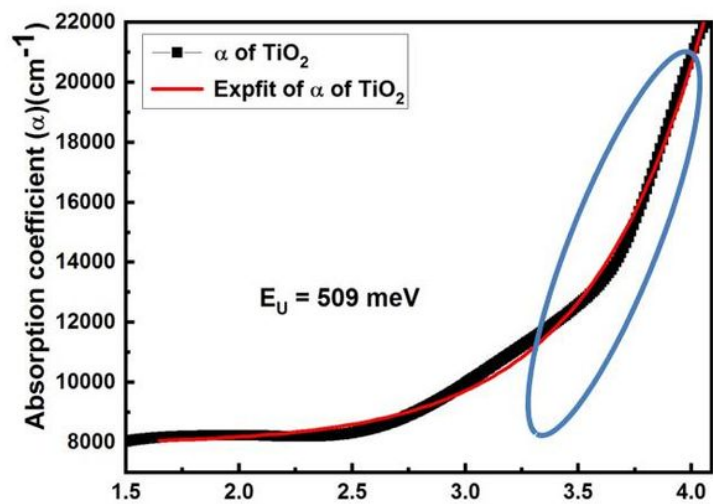
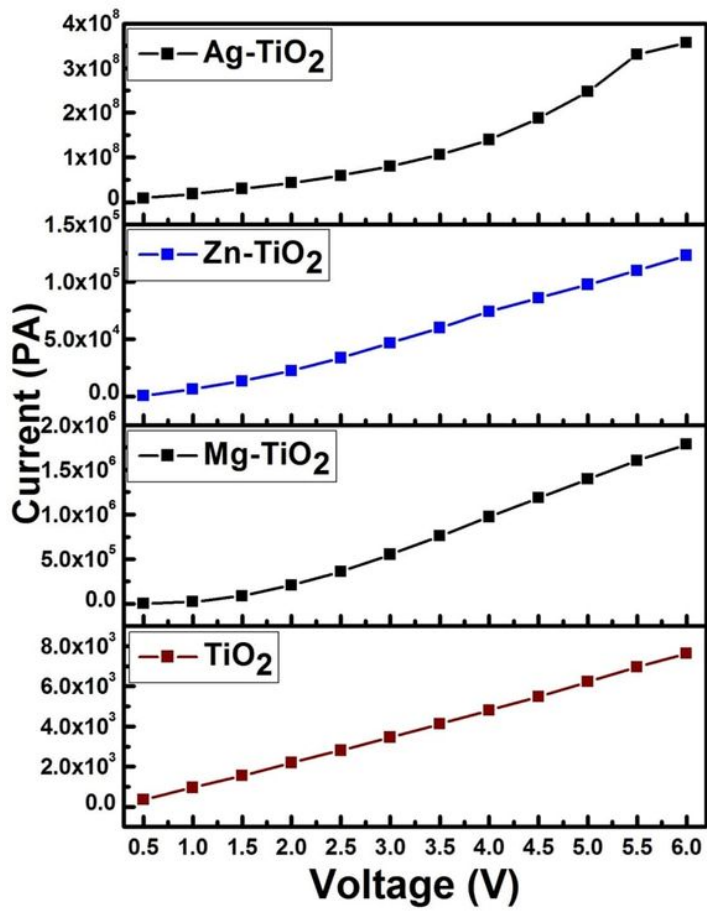
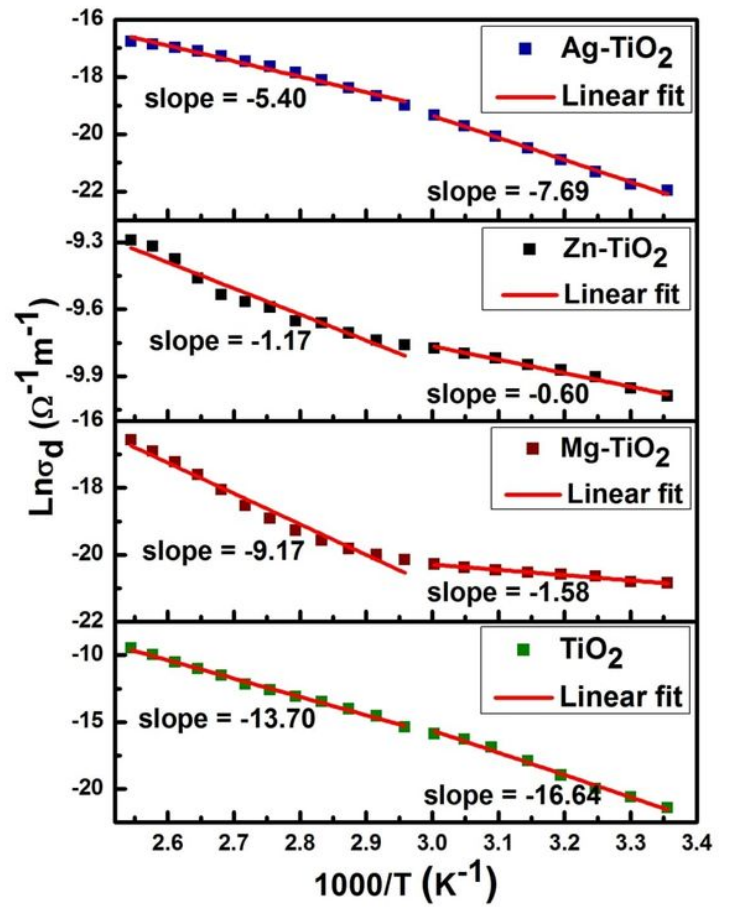


Figure 6

Plot of α with $h\nu$.



(a)



(b)

Figure 7

(a) I-V characteristics. (b) $\ln\sigma_{dc}$ versus $1000/T$ plot in (338 K - 393 K) and (298 K - 338 K) temperature range.

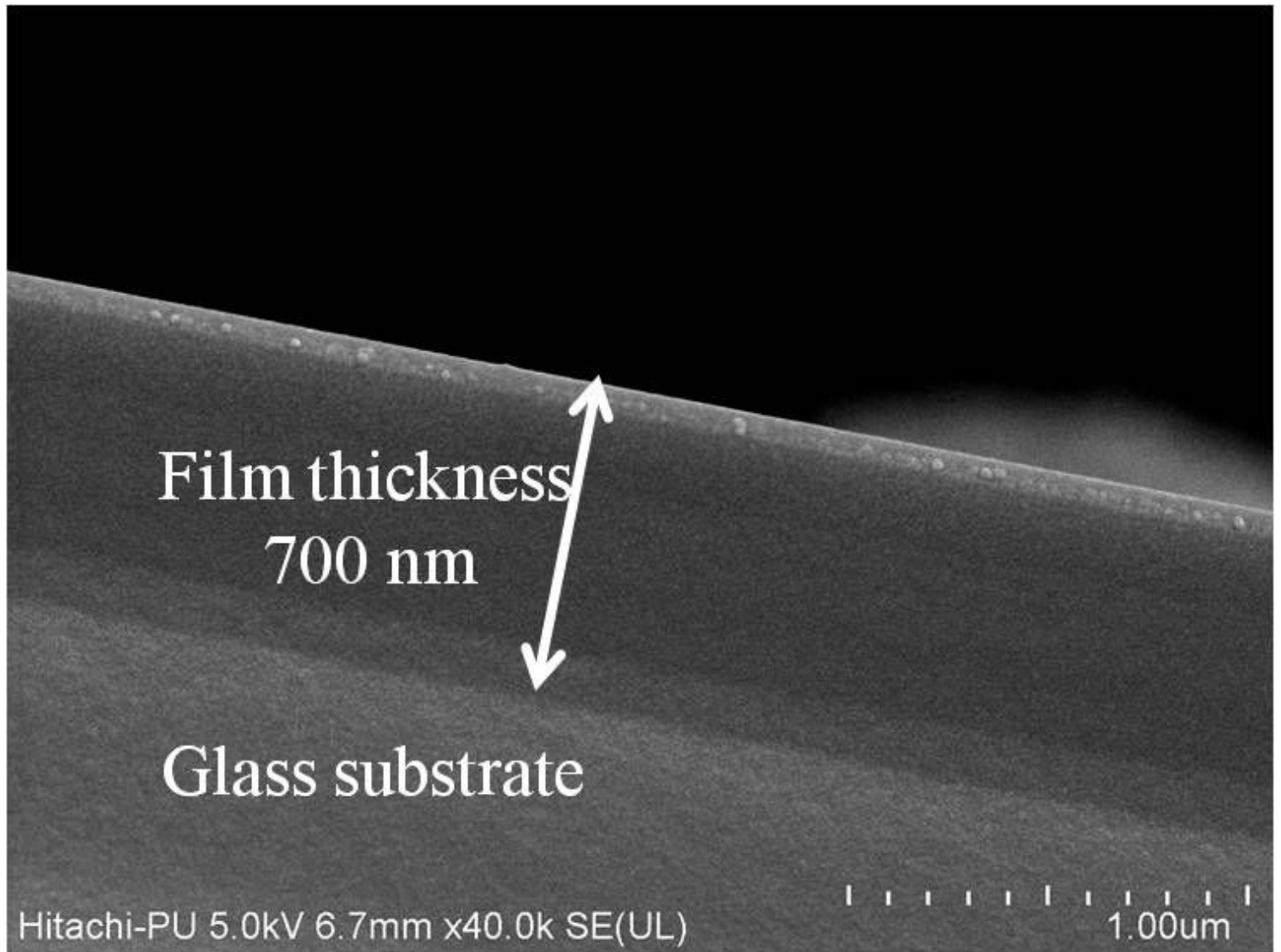


Figure 8

Cross-section of the film.

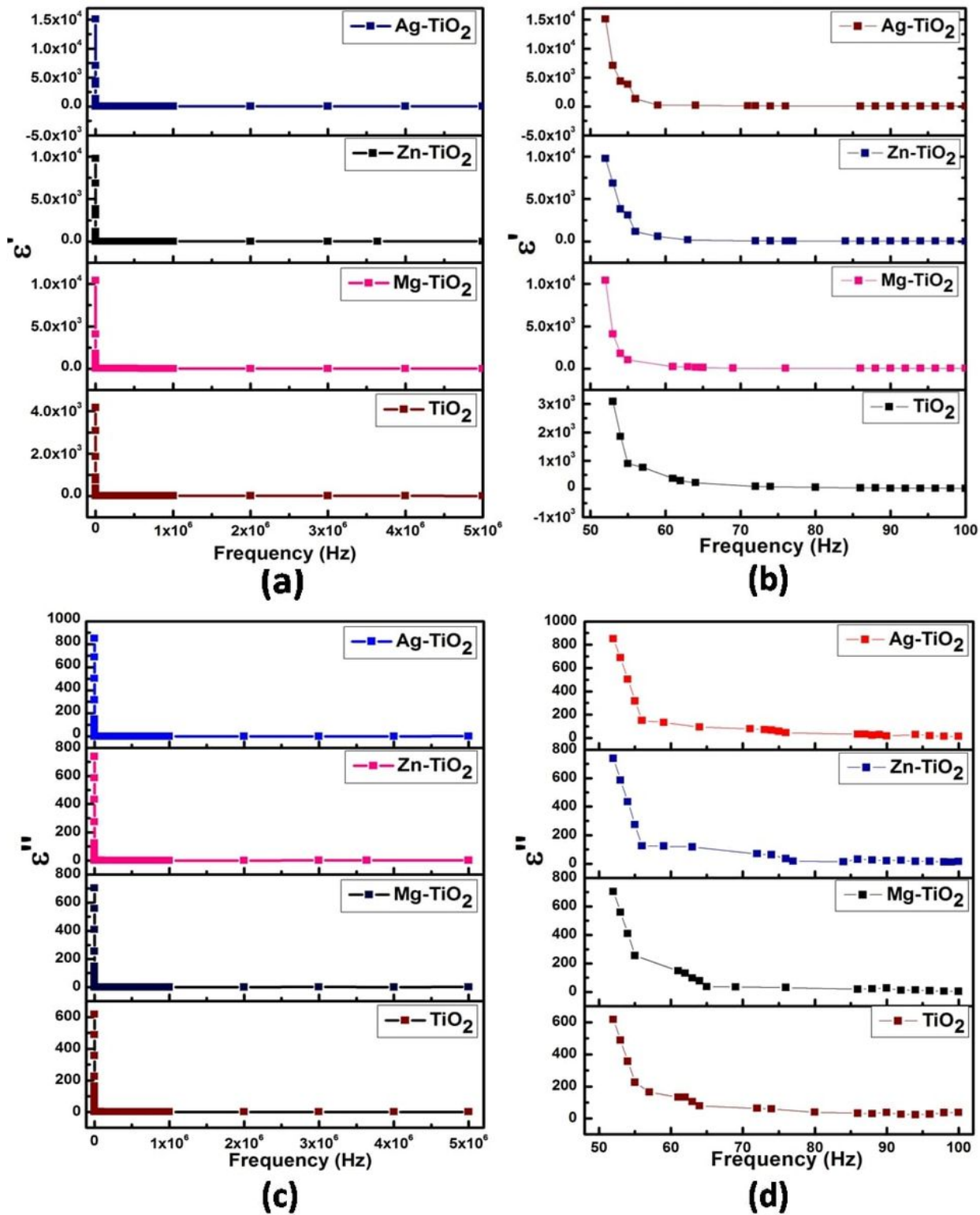


Figure 9

(a) ϵ' versus frequency variation (50 Hz -5 MHz). (b) ϵ' versus frequency variation. (c) ϵ'' versus frequency variation (50 Hz - 5 MHz). (d) ϵ'' versus frequency variation.

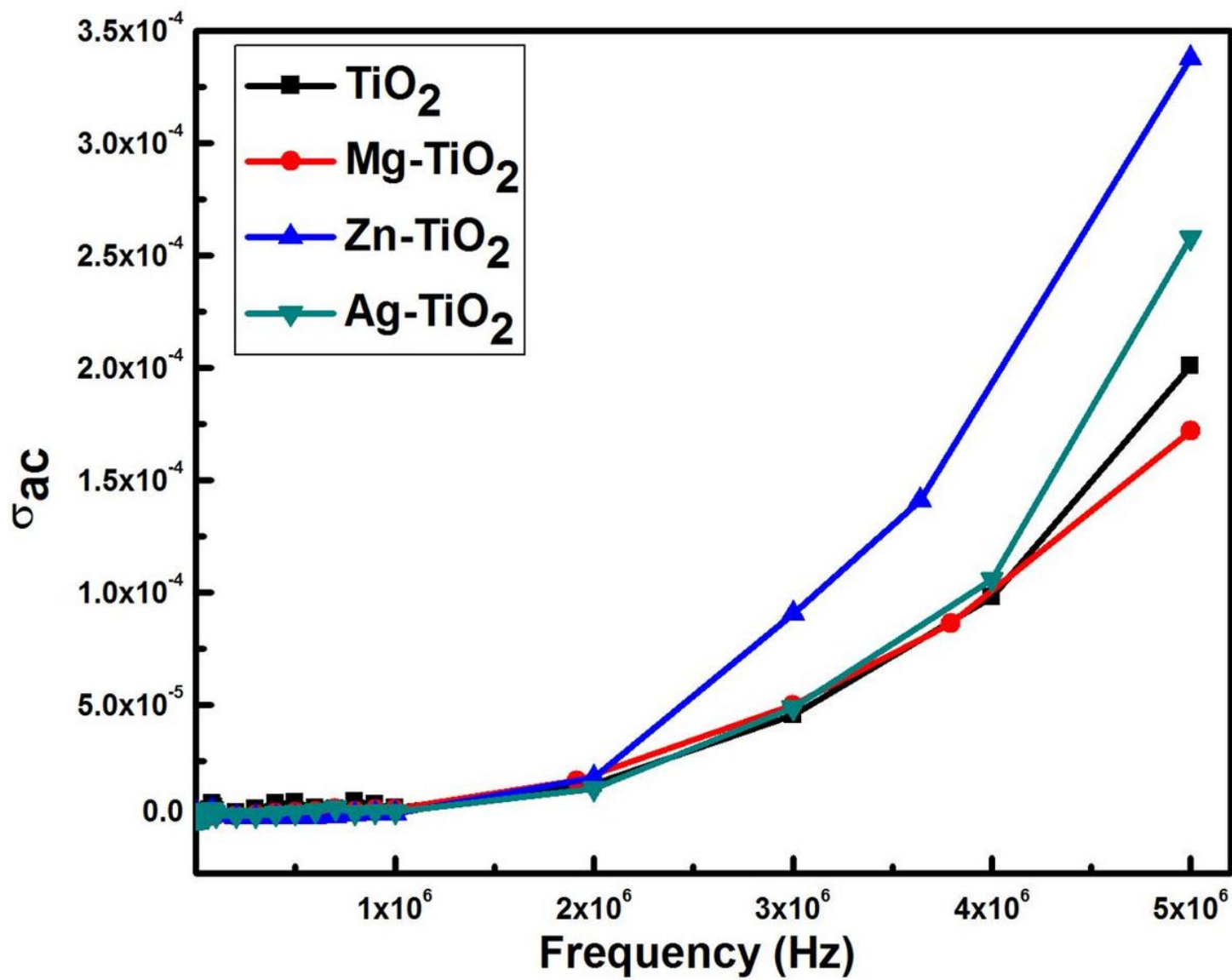


Figure 10

σ_{ac} versus 'f' plot.

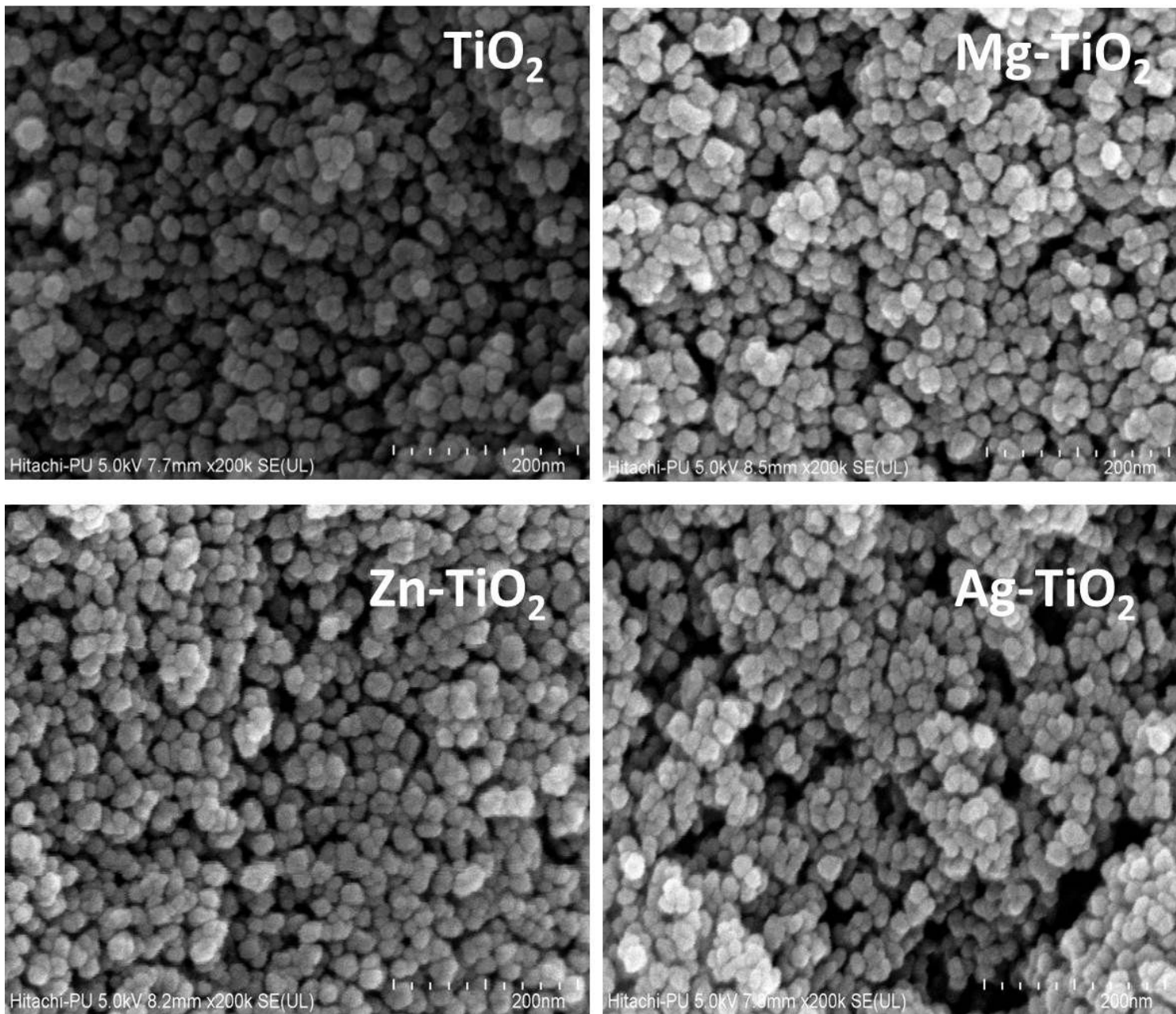


Figure 11

Surface morphology of TiO₂, Mg- TiO₂, Zn- TiO₂ and Ag- TiO₂.

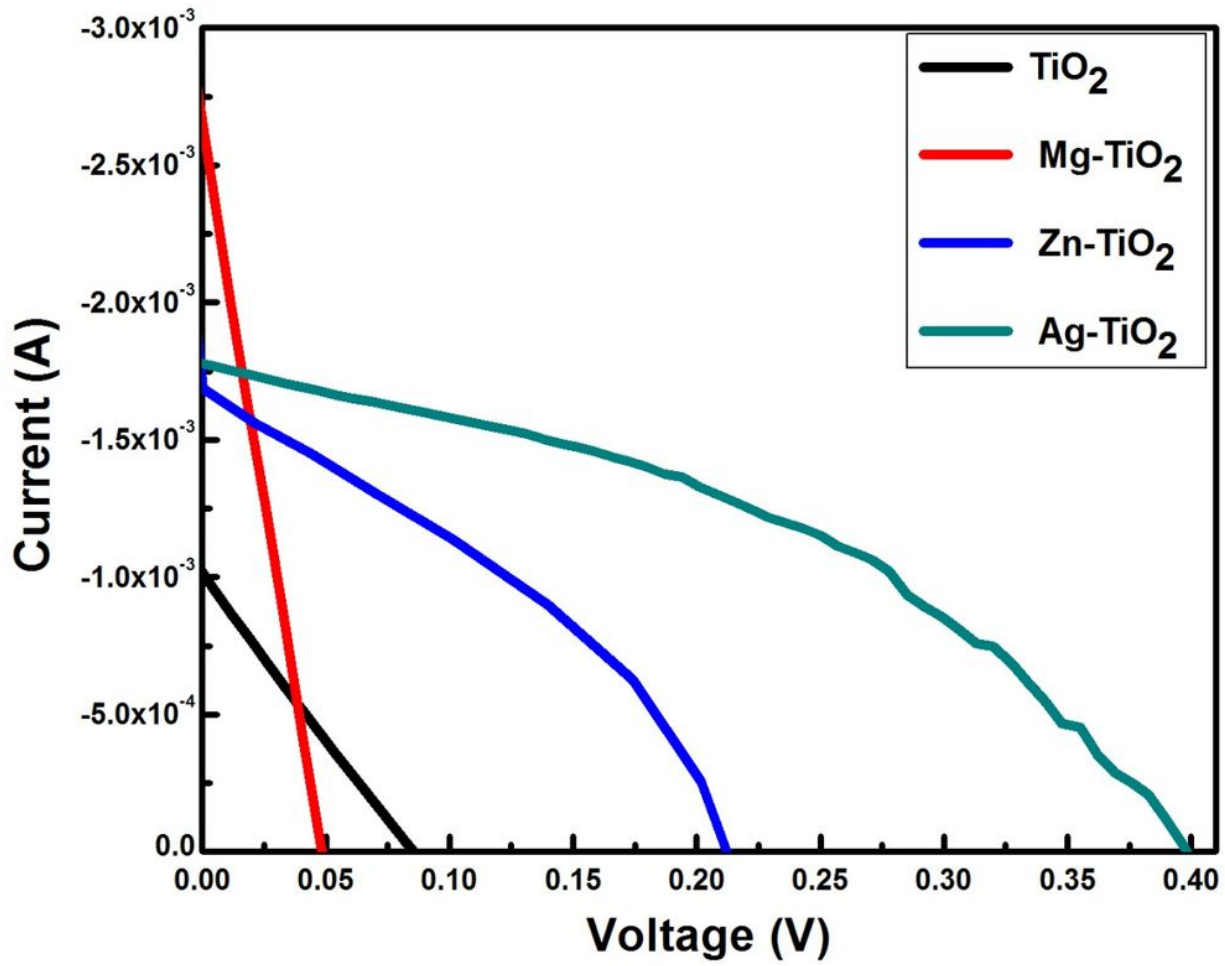


Figure 12

I-V plots of device (a), (b), (c) and (d).